ELECTRONIC PROPERTIES OF ARTIFICIAL GRAPHENE NANOSTRUCTURE

A Thesis Submitted to
the Graduate School of
İzmir Institute of Technology
in Partial Fulfillment of the Requirements for the Degree of

MASTER OF SCIENCE

in Physics

by
Emre Okcu

December 2021
İZMİR

Anneme ...

ACKNOWLEDGMENTS

I would like to thank to my supervisor A.Devrim GÜÇLÜ for all support. He is every time being polite and also acting like a brother. He always shows me the ways to improve my scientific behavior. And my family especially my lovely mother and sister. My mother is always supportive and being a good role model to me. I would also like to thank my committee members, Prof. Dr. Serpil ŞAKİROĞLU and Prof. Dr. R. Tuğrul SENGER. Also, I would like to thanks my group mates Erdoğan Bulut KUL and Gökhan ÖZTARHAN, especially Erdoğan Bulut KUL for being a good friend to me.

This work was supported by The Scientific and Technological Research Council of Turkey (TUBITAK) under the 1001 Grant Project No.119F119.

ABSTRACT

ELECTRONIC PROPERTIES OF ARTIFICIAL GRAPHENE NANOSTRUCTURE

Artificial graphene is an artificial honeycomb structure which mimics the interesting properties of graphene. Such as Dirac cone in energy dispersion, zero band gap etc. Wide range of production type makes artificial graphene valuable material. It can be engineered by lasers, molecules, and semiconductors. Semiconductor based artificial graphene can be produced by dot lattice with honeycomb patterned attractive potential or by antidot lattice with triangular patterned repulsive potential. In the following calculations, semiconductor (GaAs) based artificial graphene was used to compute electronic properties.

Like in graphene, artificial graphene has Dirac cones in energy dispersion. However, graphene has 1.42 Å carbon to carbon atom distance. This distance can not be changed but artificial graphene offers us tunability. Different parameters yield tons of band structure. It offers not only Dirac cone but also gaped bands in energy dispersion. This graphene-like feature and tunability make artificial graphene an important and researchable subject. Besides, we added another tunable parameter stiffness to control the shape of potential. Stiffness became another important parameter in our calculations. We observed that stiffness dramatically changes the band structure of the material.

As a first step, artificial graphene band structures are calculated from the single-electron approximation. Some parameters are compared with other works and the same results are found. Dirac cones are achieved in band structures. Hopping and Hubbard U values are computed. Those parameters are essential for computing finite structures. Mean-field Hubbard can be solved, and wave functions can be used as input for input required methods such as quantum Monte Carlo.

As a second step, we used the density functional theory method to investigate electron-electron interactions. Local density approximation was chosen to solve the Kohn-Sham equation. Hopping parameters obtained from DFT are much realistic than the single-electron approximation. Stiffness plays a big role in DFT energy dispersion. Different stiffness values result in different band structures. Those stiffness values influence Dirac cones and their slope. So that stiffness changes the hopping parameter.

ÖZET

YAPAY GRAFEN NANOYAPILARININ ELEKTRONİK ÖZELLİKLERİ

Yapay grafen, yapay bal peteği simetrisiyle grafenin dikkat çeken özelliklerini taklit eder. Örneğin; Enerji dağılımında Dirac konileri, sıfır bant aralığı gibi. Çok yönlü üretim metodları yapay grafeni değerli malzeme yapmaktadır. Lazerler, moleküller ve yarı iletkenlerle üretilebilinir. Yarı iletken temelli yapay grafen çekici potansiyel ile balpeteği deseniyle nokta örgüyle ya da itici potansiyel ile üçgen deseniyle antinokta örgüyle üretilebilinir. Hesaplamalarda yarıiletken (GaAs) temelli yapay grafen kullanılarak elektronik özellikler hesaplandı.

Grafendeki gibi yapay grafen de enerji dağılımlarında Dirac konilerine sahiptir. Grafenin karbon atomları arası mesafesi 1.42 Ådur. Bu mesafe değiştirilemez fakat yapay grafen bize ayarlanabilirlik sağlamaktadır. Farklı parametreler fazlasıyla bant yapısı sağlamaktadır. Sadece Dirac konileri değil aynı zamanada boşluklu bant yapılarını da sağlamaktadır. Grafenimsi özellikler ve ayarlanabilirlilik yapay grafeni önemli ve araştırmaya değer kılmaktadır. Bunun yanında başka ayarlanabilir parametre olan sertlik potansiyelin şeklini değiştirmek için ekledik. Sertlik hesaplarımızda önemli bir parametre oldu. Sertlik bant yapısı üzerinde dramatik değişimlere neden oldu.

Öncelikle, tek-elektron yakınsamasıyla yapay grafenin bant yapıları hesaplandı. Bazı parametreler diğer çalışmalarla karşılaştırıldı ve aynı sonuçlar bulundu. Dirac konileri enerji dağılımda elde edildi. Hoplama ve Hubbard U parametreleri hesaplandı. Bu parametreler sonlu yapıları hesaplamak için önemlidir. Ortalama-alan Hubbard denklemi çözülüp dalga fonksiyonları deneme dalga fonksiyonu olarak kuantum Monte Carlo gibi metodlarda kullanilabilinir.

İkinci adım, yoğunluk fonksiyon teorisi kullanarak elektron-elektron etkileşimleri hesaplandı. Yerel yoğunluk yakınsaması Kohn-Sham denklemini çözmek için seçildi. YFT'den elde edilen hoplama parametreleri tek-elektron yakınsamasına göre daha gerçekçidir. YFT'de sertlik enerji dağılımda önemli rol oynamaktadır. Farklı sertlik değerleri farklı bant yapılarına neden olmaktadır. Bu sertlik Dirac konileri ve eğimlerine etki etmektedir. Bu yüzden sertlik hoplama parametresini değiştiren bir parametredir.

TABLE OF CONTENTS

LIST OF FIGURES

Figure **Page**

Figure **Page**

LIST OF TABLES

Table **Page**

LIST OF ABBREVIATIONS

DFT . . . . . Density Functional Theory

2D . . . . . Two Dimensional

3D . . . . . Three Dimensional

QMC . . . . . Quantum Monte Carlo

nm . . . . . Nanometer

CHAPTER 1

INTRODUCTION

Graphene is a 2D material made of carbon atoms with honeycomb lattice and one atomic layer thickness (Novoselov et al. (2004)). First theoretical examination was held by Wallace using the tight-binding method and he found that graphene has semi-metallic property and it has Fermi velocity about 10^6 m/s (Wallace (1947);Castro Neto et al. (2009)) and also massless Dirac fermions act like relativistic particle (Castro Neto et al. (2009)). Geim and Novoselov made graphene films by mechanical exfoliation and they were awarded Nobel prize in 2010 (Novoselov et al. (2004)) There are several methods to obtain graphene besides mechanical exfoliation i.e. chemical vapor deposition (Juang et al. (2010);Reina et al. (2009)), thermal decomposition of SiC (Berger et al. (2004)).

Graphene is elastic and rigid under high pressure (Lee et al. (2008); Bunch et al. (2008)). Thermal conductivity experimentally revealed (Balandin et al. (2008)) that at room temperature exceed 5,300 W/mK (Guclu A.D. (2014)).

Graphene has sp^2 hybridization and each carbon atom has four electrons, three of them bounded to other carbon atoms fourth one is not bonded (Castro Neto et al. (2009)). Three bounded electrons form up σ bond, The other electron made π bond. Those bonds cause trigonal planar formation that results in a honeycomb lattice. The finite structure of graphene's geometry and edge differences makes various electronic and magnetic properties. Graphene quantum dots can be a zigzag or armchair edge with triangular structure or hexagonal structure and size, edge, and shape dependence result in different energy spectrum (Guclu A.D. (2014)).

Graphene has crystal impurities and defects on the lattice (Hashimoto et al. (2004)), scientists are investigating this problem. There are several articles for impurities and defects and these articles about how to avoid them (Tian et al. (2017)) or how these affect to physical properties (Radchenko et al. (2014); Savvas and Stefanou (2018);Kul et al. (2020)).

The application of graphene in various fields makes it a valuable material. Graphene-

based semiconductors can be used like silicon field-effect transistors (Ihn et al. (2010)). Another field is medicine. The graphene-based antimicrobial coating is an interesting topic because of microbial resistance (Staneva et al. (2021)). Fighting cancer (Fiorillo et al. (2015)) and numerous applications (Priyadarsini et al. (2018)) are some of them.

Distance between two carbon atoms is 1.42 Å (Wallace (1947);Castro Neto et al. (2009)). Unfortunately, nature does not allow us to change this distance but fortunately, artificially made atoms (dots) can change the destiny of graphene. Artificial graphene is also 2D material engineered from semiconductors (Manfra et al. (2015)), molecules (Gomes et al. (2012)) or laser (Wunsch et al. (2008)). Semiconductor based artificial graphene can be built with honeycomb structure by using dot lattice (Wang et al. (2017)) with attractive potential or triangular structure by using antidot lattice (Du et al. (2018)) with repulsive potential. It has great flexibility due to tunable parameters. Those parameters give the opportunity to have band structure with Dirac cones for different radius, potential, and dot to dot or antidot to antidot distances. In this work, we used semiconductor-based material made of GaAs.

The starting point of single-electron approximation is to find the suitable reciprocal lattice vectors from honeycomb lattice vectors (Castro Neto et al. (2009)) and triangular lattice vectors (Marder (2010)). Reciprocal lattice vectors can be obtained by the cross-product of graphene lattice vectors (Ashcroft and Mermin (1976)). The k vectors should be obtained by related G vectors (Ashcroft and Mermin (1976)). Writing down the Scrödinger's equation and taking the Fourier transformation yields the momentum space Scrödinger's equation (Ashcroft and Mermin (1976)). The tangent-hyperbolic function which used in the potential is slowly varying to zero, therefore 6 dots and 4 antidots were used to obtain the nearest neighborhood effect. The procedure of solving Scrödinger's equation is diagonalizing the equation for each k point and resulting energies build the band structure. The famous Band structure of graphene has Dirac cones (Guclu A.D. (2014)) hence, not surprisingly artificial graphene has this feature. The entire thesis is based on how different distances, radius, and potential values of dots and antidots affect band energies.

Another important point is the hopping parameter t (Castro Neto et al. (2009)) and Hubbard U (Kaxiras (2003)). Those parameters are important for examining the magnetic properties, especially in order to calculate the Hubbard equation. The slope of the second

band close to the Dirac point yields the t parameter. One of the easiest ways to calculate the U parameter is by writing down the integral as elliptic integral (Arfken and Weber (2005)) then solving numerically.

The second part is DFT. There are a lot of DFT methods out there (Parr and Yang (1989)). We choose the local density approximation to compute many-electron effects. This method was first introduced by Hohenberg and Kohn in 1964 (Hohenberg and Kohn (1964)). They propose that summation of kinetic energy and electron-electron interaction energies are functional of charge density (Hohenberg and Kohn (1964); Bagayoko (2014)). Also, they state that electron density is written in terms of ground-state wave functions. The important points in DFT calculations is the self-consistent method and exchange-correlation potential. Kohn and Sham published an article that consists of self-consistent method and exchange and correlation effects (Kohn and Sham (1965)). These two articles build the fundamentals of DFT. Using that information, adding Coulomb potential and exchange-correlation potential (Tanatar and Ceperley (1989)) in Hamiltonian results the Kohn-Sham equation (Parr and Yang (1989)). Obtaining exchange-correlation potential is simply taking the functional derivative of exchange and correlation energy with respect to the charge density. The electron charge density is the ground-state wave function square. Coulomb and exchange-correlation potential is a function of charge density, for each k point charge densities are calculated then Coulomb and exchange-correlation potential are found. These calculations are held in the self-consistent loop until the energies are the same.

CHAPTER 2

METHOD OF THEORETICAL CALCULATION

In this section, starting from the periodicity of potential, which is V, by writing down the Schrödinger's equation in momentum space to acquire single-electron energies. Those energies are used to obtain band structure and hopping parameter t values. After that, a single dot is modeled to find the approximate value of Hubbard U values. DFT method was applied to investigate the many-electron properties of Artificial Graphene. Same as single-electron case, band structures, and t values calculated.

2.1. Single-Electron Approximation

2.1.1. Bloch's Theorem

The potential of dot or antidot is periodic over the all space $V(\vec{r}+\vec{R}) = V(\vec{r})$ so that also wave function is also periodic $\psi_{nk}(\vec{r}) = e^{i\vec{k}\cdot\vec{r}}c_{nk}(\vec{r})$ and $c_{nk}(\vec{r}+\vec{R}) = c_{nk}(\vec{r})$ using this properties the wave function is $\psi_{nk}(\vec{r}+\vec{R}) = e^{i\vec{k}\cdot\vec{R}}\psi_{nk}(\vec{r})$ (Ashcroft and Mermin (1976)) . Bloch's theorem allows calculation over unit cell instead of entire dots or anti-dots. Choosing suitable unit cell is slicing the lattice to a minimum area that can produce lattice when the area repeats over the space. By using Bloch's theorem the Schrödinger's equation can be written in momentum space (Ashcroft and Mermin (1976)). The equation which used in algorithm is (Gibertini et al. (2009)):

$$det[[\frac{\hbar}{2m_b}(\vec{k}+\vec{G})^2 - E_n(k)]\delta_{G,G'} + V(\vec{G}-\vec{G}')] = 0. \tag{2.1}$$

All G vectors can be produced by using $G = l\vec{g_1} + p\vec{g_2}$ where l and p are integer. The m_b is $0.067m$ where m is bare electron mass in vacuum (Gibertini et al. (2009)).

2.2. Dot Lattice

First thing is writing the graphene lattice vectors (Castro Neto et al. (2009)). The a is dot to dot distance:

$$\vec{a_1} = \frac{a}{2}(1, \sqrt{3}) \quad , \quad \vec{a_2} = \frac{a}{2}(1, -\sqrt{3}). \tag{2.2}$$

Resulting reciprocal lattice vectors can be calculated by using equation 2.2 (Ashcroft and Mermin (1976)):

$$\vec{g_1} = 2\pi \frac{(\vec{a_2} \times \vec{a_3})}{\vec{a_1} \cdot (\vec{a_2} \times \vec{a_3})} \quad , \quad \vec{g_2} = 2\pi \frac{(\vec{a_3} \times \vec{a_1})}{\vec{a_1} \cdot (\vec{a_2} \times \vec{a_3})}. \tag{2.3}$$

Note that $\vec{a_3}$ is a unit vector along the z axis. The resulting Reciprocal lattice vectors are:

$$\vec{g_1} = \frac{2\pi}{3a}(1, \sqrt{3}) \quad , \quad \vec{g_2} = \frac{2\pi}{3a}(1, -\sqrt{3}). \tag{2.4}$$

The next step is finding the size of the unit cell area and k points. Unit cell area is derived from equation 2.2 that is:

$$\Omega = \frac{a^2}{2} 3\sqrt{3}. \tag{2.5}$$

The k vectors can be found by following equation (Ashcroft and Mermin (1976)):

$$\vec{k} = \sum_{i=1}^{2} \frac{m_i}{N} \vec{g_i}. \tag{2.6}$$

The m_i is integer and N is total site. Using equation 2.2 and 2.6, dot lattice k vectors can be written as:

$$\vec{k} = \frac{m_1}{N}\frac{2\pi}{3a}(1,\sqrt{3}) + \frac{m_2}{N}\frac{2\pi}{3a}(1,-\sqrt{3}), \tag{2.7}$$

$$k_x = (m_1 + m_2)\frac{2\pi}{3aN}, \tag{2.8}$$

$$k_y = (m_1 - m_2)\frac{2\pi\sqrt{3}}{3aN}. \tag{2.9}$$

We modeled the potential from tangent-hyperbolic function which is $V(\vec{r}) = \frac{(V_0)}{2}(\tanh((r-a)s) - \tanh((r+a)s))$. Potential consist subtraction of two tangent-hyperbolic function. As can be seen in Figure 2.1 different stiffness value changes minimum value of potential. The parameter s controls the stiffness of function. If $s = 100$ the potential turns into cylindrical shape. For different s values the minimum point of potential varies. If $s = 100$ and $V_0 = -10$ the minimum value of potential is -10 but if $s = 0.1$ minimum value is greater than -10.

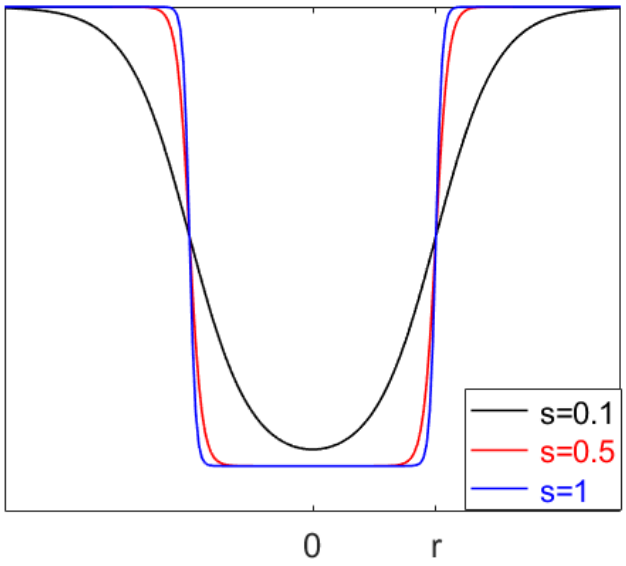

Figure 2.1. Comparison some s values.

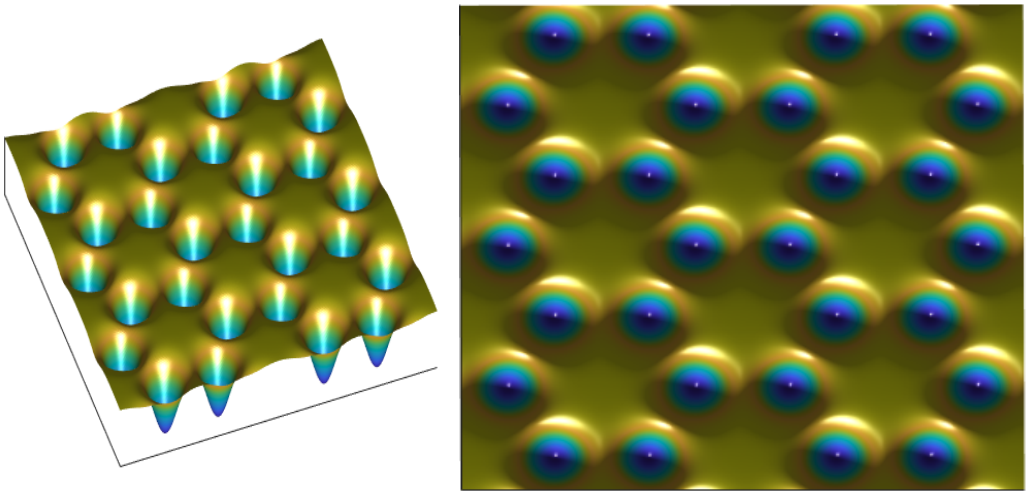

Figure 2.2. Dots with tangent-hyperbolic potential.

For $a = 150$ nm,$r = 52.5$ nm $V_0 = -0.8$ meV, resulting energies are calculated and shifted upward 0.5 meV then the energy bands are:

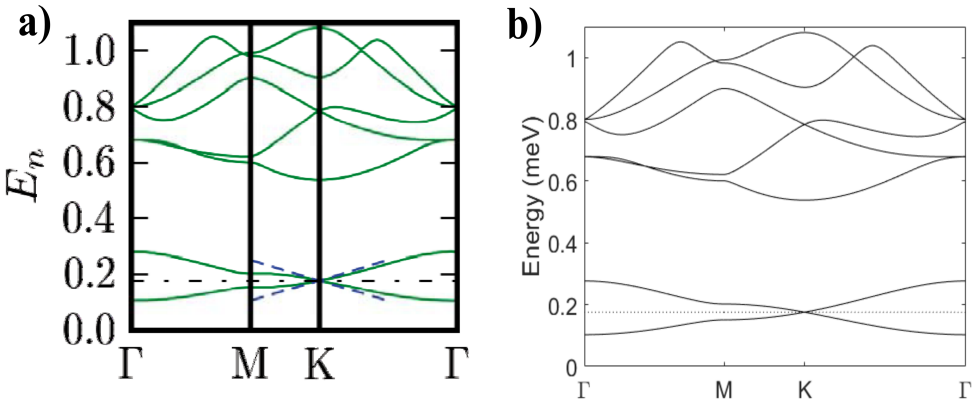

Figure 2.3. a) Band structure of artificial graphene with a dot. b) Calculated band structure from the algorithm which we wrote.
(Source: [a)] Gibertini et al. (2009))

2.3. Antidot Lattice

Antidot lattice is consist of repulsive potential with triangular symmetry. From work of Du et al. (2018) antidot lattice is suitable to have band structure which consist Dirac cones. The triangular (hexagonal) lattice vectors (Marder (2010)) are:

$$\vec{b_1} = \frac{b}{2}(\sqrt{3}, 1) \quad , \quad \vec{b_2} = \frac{b}{2}(\sqrt{3}, -1). \tag{2.10}$$

Using triangular lattice vector, reciprocal lattice vector can be calculated by equation 2.3. The reciprocal lattice vectors are:

$$\vec{g_1} = \frac{2\pi}{b}(\frac{1}{\sqrt{3}}, 1) \quad , \quad \vec{g_2} = \frac{2\pi}{b}(\frac{1}{\sqrt{3}}, -1). \tag{2.11}$$

Unit cell area can be calculated by equation 2.11.

$$\Omega = \frac{b^2}{2}\sqrt{3}. \tag{2.12}$$

The k vectors of antidot lattice by using equation 2.11 are :

$$\vec{k} = \frac{m_1}{N}\frac{2\pi}{b}(\frac{1}{\sqrt{3}}, 1) + \frac{m_2}{N}\frac{2\pi}{b}(\frac{1}{\sqrt{3}}, -1), \tag{2.13}$$

$$k_x = (m_1 + m_2)\frac{2\pi}{\sqrt{3}bN}, \tag{2.14}$$

$$k_y = (m_1 - m_2)\frac{2\pi}{bN}. \tag{2.15}$$

All information needed to solve Schrödingers equation (equation (2.1)) is known. Potential function is tangent-hyperbolic and to resemble the honeycomb structure potential is repulsive.

In Figure 2.4 b is antidot to antidot distance, r is anti dot radius and a is distance between center of honeycomb pattern with $a = \frac{b}{\sqrt{3}}$ (Du et al. (2018)). As can be seen in Figure 2.4, White circles represent the antidots with repulsive potential. Black circles define honeycomb pattern.

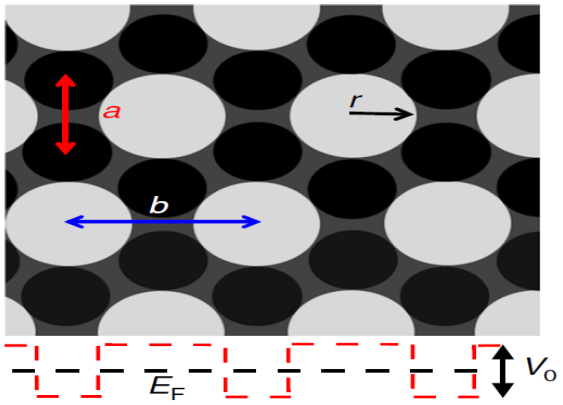

Figure 2.4. Antidot structure. .
(Source: Du et al. (2018))

For $b = 70$ nm, $r = 20$ nm $V_0 = 6$ meV, resulting energies are calculated and energies fixed up the lowest energy is zero. The energy bands are:

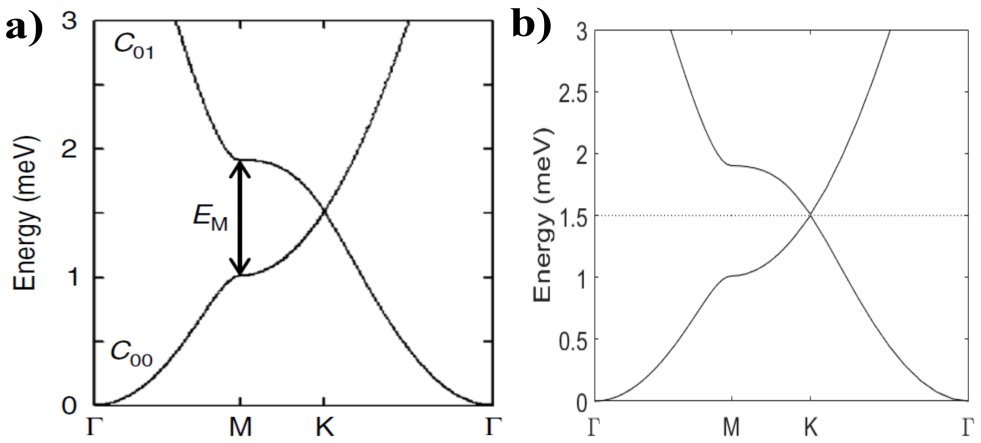

Figure 2.5. a) Band structure of artificial graphene with antidot. b) Calculated band structure from algorithm which we wrote.
(Source: [a)] Du et al. (2018))

2.4. Calculation of t and U

Hopping parameter, denoted as t, is derived from electron velocity near the K point. Velocity of electron is derivative of energy with respect to the $\vec{k}$ and dividing by $\hbar$. Hopping parameter t is:

$$\upsilon = \frac{1}{\hbar}\frac{dE}{d\vec{k}}, \qquad t = \frac{2\upsilon\hbar}{3a}. \tag{2.16}$$

Another representation of t is:

$$t = \frac{2}{3a}\frac{dE}{d\vec{k}}. \tag{2.17}$$

For calculating Hubbard U parameter first writing Schrödinger's equation in cylindrical coordinates for one dot:

$$\nabla^2 = \frac{1}{\rho}\frac{\partial}{\partial\rho}(\rho\frac{\partial}{\partial\rho}) + \frac{1}{\rho^2}(\frac{\partial^2}{\partial\phi^2}). \tag{2.18}$$

$$H = \frac{-\hbar^2}{2m_b}(\frac{1}{\rho}\frac{\partial}{\partial\rho}(\rho\frac{\partial}{\partial\rho}) + \frac{1}{\rho^2}(\frac{\partial^2}{\partial\phi^2})) + V(\rho). \tag{2.19}$$

The wave function has radial and angular part which can be written as:

$$\psi = R(\rho)\Phi(\phi). \tag{2.20}$$

Schrödinger's equation is:

$$H\psi = E\psi, \tag{2.21}$$

$$\frac{-\hbar^2}{2m_b}(\frac{1}{\rho}\frac{d}{d\rho}(\rho\frac{dR}{d\rho})\Phi + \frac{R}{\rho^2}(\frac{d^2\Phi}{d\phi^2})) + (V(\rho) - E)R\Phi = 0. \tag{2.22}$$

Multiplying by $\frac{1}{R\Phi}$ results two differentiable equation, first one is angular equation. An-

gular equation has azimuthal symmetry which is:

$$\frac{1}{\Phi}\frac{d^2\Phi}{d\phi^2} = -l^2, \tag{2.23}$$

$$\Phi(\phi) = e^{-l\phi} \quad l = 0, \pm 1, \pm 2, ... \tag{2.24}$$

and the radial equation is:

$$\rho^2\frac{d^2R}{d\rho^2} + \rho\frac{dR}{d\rho} - l^2R - \frac{2m_b\rho^2}{\hbar^2} + (V(\rho) - E)R = 0. \tag{2.25}$$

the potential which we modeled is $V(\vec{\rho}) = \frac{(V_0)}{2}(\text{tanh}((\rho - a)s) - \text{tanh}((\rho + a)s))$. Solving analytically equation 2.25 is impossible so that numerical solution is the only way to obtain solutions. Ground-state wave functions are needed for calculating electron density. When $l = 0$, solutions consist of only ground state wave functions. Strategy for calculating numerically Hubbard U parameter involves two steps:

i) Calculate electron's potential by using charge density.

ii) Integration of charge density times electron's potential gives the Hubbard U

This way is not a self-consistent way to obtain Hubbard U parameters but at least gives us a clue about approximate values. The path that we followed for this process is solving Schrödinger's equation numerically for a single dot in a loop to obtain minimum energy. The ground-state wave function square yields the electron density which is $n(r)$. Writing the potential and proceeding results:

$$V_e(r_0) = \int \frac{n(r)rdrd\theta}{|\vec{r} - \vec{r_0}|}, \qquad r_0//\hat{x}, \tag{2.26}$$

$$V_e(r_0) = \int \frac{n(r)rdrd\theta}{\sqrt{r_0^2 + r^2 - 2rr_0cos\theta}} = \int n(r)rdr\boldsymbol{I}_\theta, \tag{2.27}$$

$$\boldsymbol{I}_\theta = \int_0^{2\pi} \frac{d\theta}{\sqrt{r_0^2 + r^2 - 2rr_0cos\theta}}, \tag{2.28}$$

$$= 2\int_0^{\pi} \frac{d\theta}{\sqrt{r_0^2 + r^2 - 2rr_0cos\theta}}, \tag{2.29}$$

$$= 2\int_0^{\pi} \frac{d\theta}{\sqrt{r_0^2 + r^2 - 2rr_0(1 - 2sin^2\frac{\theta}{2})}}, \tag{2.30}$$

$$= 4\int_0^{\frac{\pi}{2}} \frac{d\theta}{\sqrt{(r_0 - r)^2 + 4rr_0 sin^2\theta}}, \tag{2.31}$$

$$= \frac{4}{|r_0 - r|}\int_0^{\frac{\pi}{2}} \frac{d\theta}{\sqrt{1 + \frac{4rr_0}{(r_0 - r)^2}sin^2\theta}}, \tag{2.32}$$

$$= \frac{4}{|r_0 - r|}K(k^2 = -\frac{4rr_0}{(r_0 - r)^2}), \tag{2.33}$$

$$V_e(r_0) = \int \frac{n(r)rdr}{|\vec{r} - \vec{r_0}|} = 4\int \frac{n(r)rdr}{|\vec{r} - \vec{r_0}|}K(k^2 = -\frac{4rr_0}{(r_0 - r)^2}). \tag{2.34}$$

$K(k^2 = -\frac{4rr_0}{(r_0 - r)^2})$ is complete elliptic integral of the 1st kind (Arfken and Weber (2005)). Another form is:

$$\boldsymbol{I}_{\theta} = 2\int_0^{\pi} \frac{d\theta}{\sqrt{r_0^2 + r^2 + 2rr_0 cos(\pi - \theta)}}, \tag{2.35}$$

$$= -2\int_{\pi}^{0} \frac{d\theta}{\sqrt{r_0^2 + r^2 + 2rr_0 cos\theta}}, \tag{2.36}$$

$$= 2\int_0^{\pi} \frac{d\theta}{\sqrt{r_0^2 + r^2 + 2rr_0(1 - 2sin^2\frac{\theta}{2})}}, \tag{2.37}$$

$$= 4\int_0^{\frac{\pi}{2}} \frac{d\theta}{\sqrt{(r_0 + r)^2 - 4rr_0 sin^2\theta}}, \tag{2.38}$$

$$= \frac{4}{|r_0 + r|}\int_0^{\frac{\pi}{2}} \frac{d\theta}{\sqrt{1 - \frac{4rr_0}{(r_0 + r)^2}sin^2\theta}}, \tag{2.39}$$

$$= \frac{4}{|r_0 + r|}K(k^2 = \frac{4rr_0}{(r_0 - r)^2}), \tag{2.40}$$

$$V_e(r_0) = \int \frac{n(r)rdr}{|\vec{r} - \vec{r_0}|} = 4\int \frac{n(r)rdr}{|\vec{r} + \vec{r_0}|}K(k^2 = \frac{4rr_0}{(r_0 + r)^2}). \tag{2.41}$$

Hubbard U parameter integral is(Kaxiras (2003)):

$$U = 2\pi \int rn(r)V_e(r)dr. \tag{2.42}$$

t and U parameters can be used in the Hubbard model to investigate finite structures. In QMC calculations initial wave function is needed so the Hubbard wave functions are also usable as an initial wave function. t and U are essential to acquire whether the system is paramagnetic or diamagnetic.

2.5. Density Functional Theory

DFT is a method to investigate electron-electron interaction problems. We used ground-state wave function square as an electron charge density which is called local density approximations (Parr and Yang (1989);Marder (2010)). DFT Hamiltonian includes kinetic energy, dot potential, Coulomb potential, and exchange-correlation potential (Tanatar and Ceperley (1989)). Coulomb and exchange-correlation potentials are a function of electron charge density. The primary objective is to find single-electron ground states to build electron charge density. Putting charge density in Coulomb and exchange-correlation potential functions then solving again yields many-electron wave functions. These wave functions are used as a charge density recursively. This iteration process should continue until the energies do not change. In this work, up and down spin numbers are equal. The DFT Hamiltonian is:

$$\begin{aligned} H = &\frac{\hbar}{2m_b}(\vec{k}+\vec{G})^2 + V_{dot}(\vec{G}-\vec{G}') + V_{coulomb}(\vec{G}-\vec{G}') \\ &+ V_{exchange}(\vec{G}-\vec{G}') + V_{correlation}(\vec{G}-\vec{G}'). \end{aligned} \tag{2.43}$$

The Fourier transformation of potential is essential because modeled potential is written in real space. Potential transform in momentum space by using equation 2.45.

$$V(\vec{r}) = \sum_G V(\vec{G}) e^{i\vec{G}\cdot\vec{r}}, \tag{2.44}$$

$$V(\vec{G}) = \frac{1}{\Omega}\int_\Omega V(\vec{r}) e^{-i\vec{G}\cdot\vec{r}} dr. \tag{2.45}$$

Coulomb interaction can be written as (Castro et al. (2009)):

$$V_{coulomb}(\vec{r}) = \int_{\infty} d^2r' \frac{n(\vec{r'})}{|\vec{r} - \vec{r'}|} = \int_{\infty} n(\vec{r'}) v(\vec{r} - \vec{r'}) d^2r'. \tag{2.46}$$

Lattice is periodic so that $V_{coulomb}$ is also periodic. From equation 2.45, we get:

$$\begin{aligned}
V(\vec{G}) &= \frac{1}{\Omega} \int_{\Omega} V(\vec{r}) e^{i\vec{G}\cdot\vec{r}} dr, && (2.47)\\
&= \frac{1}{\Omega} \int_{\Omega} \int_{\infty} d^2r', e^{-i\vec{G}\cdot\vec{r}} e^{i\vec{G}\cdot\vec{r'}} e^{-i\vec{G}\cdot\vec{r'}} n(\vec{r'}) v(\vec{r} - \vec{r'}), && (2.48)\\
&= \frac{1}{V} \int_{\infty} d^2r \int_{\infty}, d^2r' e^{-i\vec{G}\cdot\vec{r'}} n(\vec{r'}) e^{-i\vec{G}\cdot(\vec{r}-\vec{r'})} v(\vec{r} - \vec{r'}), && (2.49)\\
&= \frac{1}{V} \int_{\infty} d^2r' e^{-i\vec{G}\cdot\vec{r'}} n(\vec{r'}) \int_{\infty} d^2r e^{-i\vec{G}\cdot(\vec{r}-\vec{r'})} v(\vec{r} - \vec{r'}), \quad (\vec{r} - \vec{r'}) \to \vec{r}, && (2.50)\\
&= n(\vec{G}) v(\vec{G}). && (2.51)
\end{aligned}$$

From equation 2.51, calculation of $v(\vec{G})$ is:

$$\begin{aligned}
v(\vec{G}) &= \int d^2r \frac{e^{-i\vec{G}\cdot\vec{r}}}{r}, && (2.52)\\
v(\vec{G}) &= \int r dr d\theta \frac{e^{-i\vec{G}\cdot\vec{r}}}{r}, && (2.53)\\
v(\vec{G}) &= \int_0^{\infty} \int_0^{2\pi} r dr d\theta e^{-i\vec{G}\cdot\vec{r}}. && (2.54)
\end{aligned}$$

Now, taking $\vec{G}//\hat{r}$ and using

$$\begin{aligned}
J_n(\vec{z}) &= \frac{1}{2\pi i^n} \int_0^{2\pi} e^{izcos\theta} e^{in\theta} d\theta, && (2.55)\\
J_0(\vec{z}) &= \frac{1}{2\pi} \int_0^{2\pi} e^{izcos\theta} d\theta, && (2.56)
\end{aligned}$$

equation 2.54 become

$$v(\vec{G}) = 2\pi \int_0^\infty dr J_0(Gr), \tag{2.57}$$

$$= \frac{2\pi}{G} \int_0^\infty du J_0(u), \tag{2.58}$$

$$= \frac{2\pi}{G}. \tag{2.59}$$

From equation 2.51, calculation of $n(\vec{G})$ is:

$$n(\vec{G}) = \frac{1}{\Omega} \int_\Omega n(\vec{r}) e^{-i\vec{G}\cdot\vec{r}} dr, \tag{2.60}$$

$$n_k(\vec{r}) = \psi_k^*(\vec{r})\psi_k(\vec{r}), \tag{2.61}$$

$$\psi_k(\vec{r}) = e^{i\vec{k}\cdot\vec{r}} u_k(\vec{r}), \tag{2.62}$$

$$= e^{i\vec{k}\cdot\vec{r}} \sum_G c_{\vec{k}-\vec{G}} e^{-i\vec{G}\cdot\vec{r}}, \tag{2.63}$$

$$n_k(\vec{r}) = \sum_{G'} \sum_{G''} c^*_{\vec{k}-\vec{G''}} c_{\vec{k}-\vec{G'}} e^{-i(\vec{G'}-\vec{G''})\cdot\vec{r}}, \tag{2.64}$$

$$n_k(\vec{G}) = \frac{1}{\Omega} \int_\Omega d^2r \sum_{G'} \sum_{G''} c^*_{\vec{k}-\vec{G''}} c_{\vec{k}-\vec{G'}} e^{-i(\vec{G}+\vec{G'}-\vec{G''})}, \tag{2.65}$$

$$= \sum_{G'} \sum_{G''} c^*_{\vec{k}-\vec{G''}} c_{\vec{k}-\vec{G'}} \frac{1}{\Omega} \int_\Omega d^2r e^{-i(\vec{G}+\vec{G'}-\vec{G''})}, \tag{2.66}$$

$$= \sum_{G'} c_{k-G'} \Big(\sum_{G''} c^*_{k-G''} \delta_{\vec{G}+\vec{G'},\vec{G''}} \Big), \tag{2.67}$$

$$= \sum_{G'} c^*_{k-(\vec{G}+\vec{G'})} c_{k-\vec{G'}}, \tag{2.68}$$

$$n(\vec{G}) = \sum_k n_k(\vec{G}). \tag{2.69}$$

Theoretically reciprocal lattice spans at infinity but practically it is impossible to compute whole lattice. Instead of calculating over all space, creating supercell with few $\vec{G}$ that computer can handle is enough to calculate band sutructure. Equation 2.68 has two vector addition, some of vectors are out of supercell but periodicity does its job again. If vector addition is out of supercell added vector can be written inside supercell. Due to periodicity, added vectors are just replica of vectors that are inside the supercell.

Exchange and correlations potentials are (Tanatar and Ceperley (1989)):

$$\varepsilon_{ex} = -\frac{4\sqrt{2}}{3\sqrt{\pi}}\sqrt{n(\vec{r})}, \tag{2.70}$$

$$\varepsilon_c = a_0 \frac{1 + a_1 x}{1 + a_1 x + a_2 x^2 + a_3 x^3}, \tag{2.71}$$

$$x = (r_s)^{\frac{1}{2}}, \qquad r_s = \frac{a}{a_0}, \qquad a = \frac{1}{\sqrt{\pi n(r)}}. \tag{2.72}$$

a_0	-0.3568
a_1	1.1300
a_2	0.9052
a_3	0.4165

Table 2.1. Correlation energy parameters.

The potentials are simply functional derivative of energies with respect to charge density.

$$E_{ex} = \int n(\vec{r})\varepsilon_{ex}(n(\vec{r}))d^2r, \tag{2.73}$$

$$V_{ex}(\vec{r}) = \frac{\delta E_{ex}}{\delta n(\vec{r})}. \tag{2.74}$$

$$E_c = \int n(\vec{r})\varepsilon_c(n(\vec{r}))d^2r, \tag{2.75}$$

$$V_c(\vec{r}) = \frac{\delta E_c}{\delta n(\vec{r})}. \tag{2.76}$$

Functional derivative of exchange and correlation potentials are:

$$\begin{aligned} V_{ex}(\vec{r}) &= \frac{\delta E_{ex}}{\delta n(\vec{r})} = \varepsilon_{ex} + n(\vec{r})\frac{\partial \varepsilon_{ex}}{\partial n(\vec{r})} = \frac{3}{2}\varepsilon_{ex}. \\ V_c(\vec{r}) &= \frac{\delta E_c}{\delta n(\vec{r})} = \varepsilon_c + n(\vec{r})\frac{\partial \varepsilon_c}{\partial n(\vec{r})}. \end{aligned} \tag{2.77}$$

Functional derivative of exchange potential can be obtained easily. But functional derivative of correlation potential a little bit harder. Easiest way to obtain correlation

potential is taking functional derivative with respect to x with multiplication of functional derivative of x with respect to charge density.

$$V_c(\vec{r}) = \varepsilon_c + n(\vec{r})\frac{\partial \varepsilon_c}{\partial n(\vec{r})} = \varepsilon_c + n(\vec{r})\frac{\partial \varepsilon_c}{\partial x}\frac{\partial x}{\partial n(\vec{r})}, \tag{2.78}$$

$$\frac{\partial \varepsilon_c}{\partial x} = \frac{a_1(1 + a_1x + a_2x^2 + a_3x^3) - (1 + a_1x)(a_1 + 2a_2x + 3a_3x^2)}{(1 + a_1x + a_2x^2 + a_3x^3)^2}, \tag{2.79}$$

$$\frac{\partial x}{\partial n(\vec{r})} = -\frac{1}{4(\pi n(\vec{r}))^{0.25}} \tag{2.80}$$

Exchange and correlation potentials are in real space. Equation 2.69 is in momentum space so that Fourier transformation needed to calculate exchange and correlation potential. The transformation turns $n(\vec{G})$ into $n(\vec{r})$, using equation 2.77 and 2.78 with $n(\vec{r})$ computing $V_{ex}(\vec{r})$ (equation 2.44) and $V_c(\vec{r})$ (equation 2.44) then back in momentum space by inverse Fourier transformation (equation 2.45) gives the last two potential to build DFT Hamiltonian.

There should be a mixing parameter in self consistent loop. Energies sometimes oscillating back and fort between two values. Mixing previously obtained density with new density is a way to exceed this problem.

$$n_{mixed}(\vec{G}) = mn_{old}(\vec{G}) + (1 - m)n_{new}(\vec{G}), \qquad m < 1 \tag{2.81}$$

From now basic principles and equations are written to solve Schrödinger's equation both single-electron approximation and DFT. The next chapters are the application of those equations and principles.

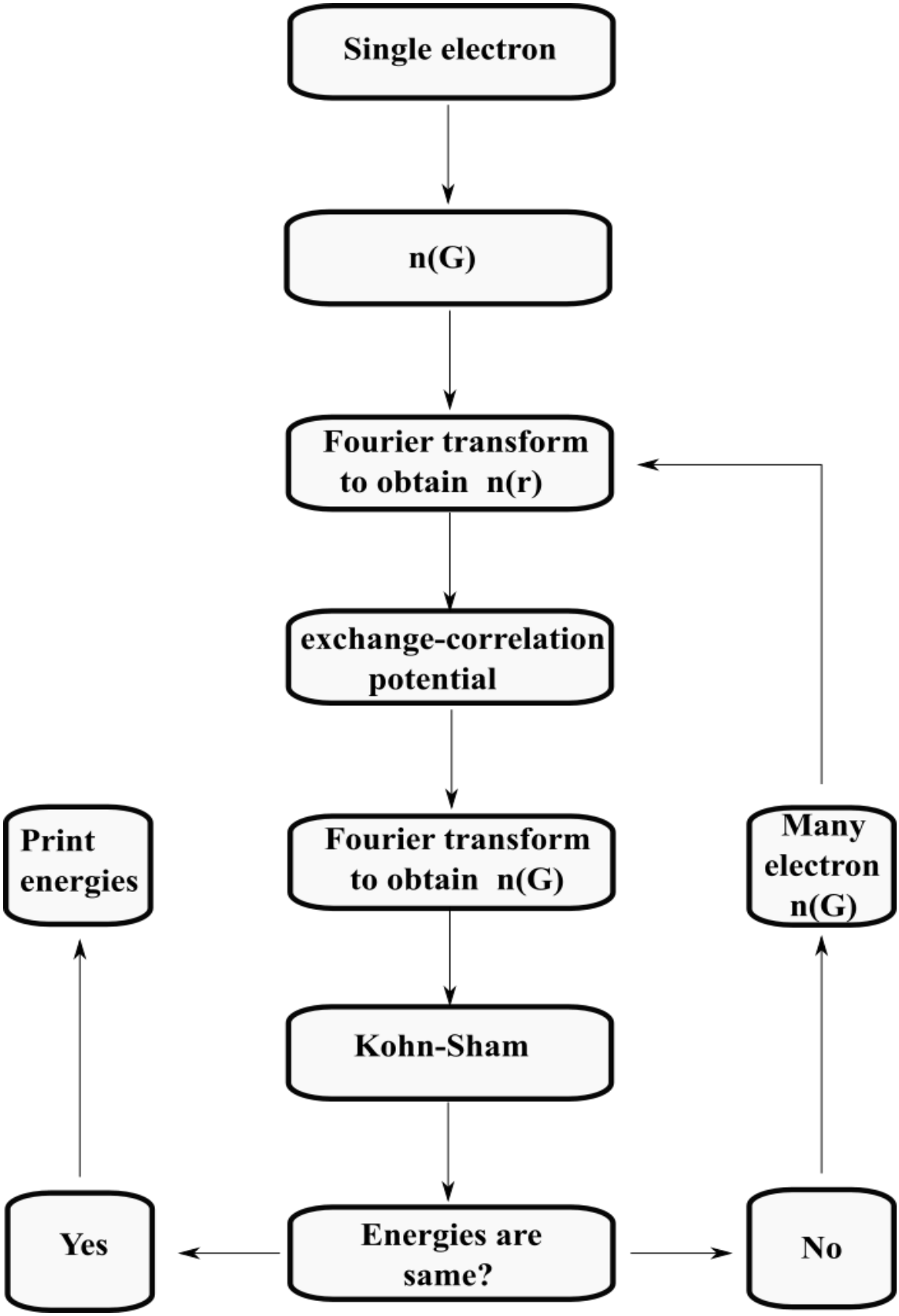

Figure 2.6. Flowchart of DFT algorithm.

CHAPTER 3

BAND STRUCTURE OF DOT LATTICE FROM SINGLE-ELECTRON APPROXIMATION

In this section, the band structure of artificial graphene with dots is examined using the single-electron approximation. Band structures are calculated for a = 50 nm and r = 5, 20, 30 nm. Potential values are V_0 = -1, -10, -40 and -70 meV. s values are 0.1, 0.5, 1. The main goal of this chapter is to understand how different parameters affect the band structure. Using equation 2.1 with equation 2.4 and equation 2.6 results in the energy of dot lattice in momentum space. In Figure 2.3, the calculated band structure of dot lattice with the algorithm which we wrote compared with another work. Adding another band structure and understanding the concept is the main theme of this chapter.

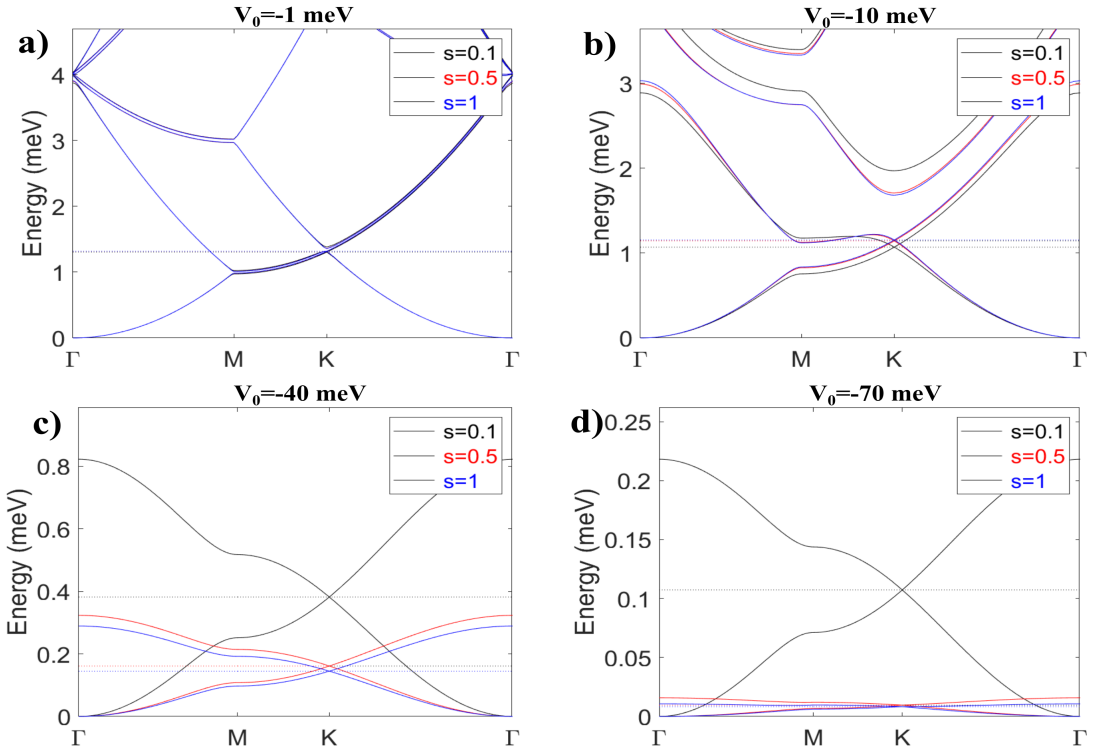

Figure 3.1. Band structures of dots with a = 50 nm, r = 5 nm. a) -1 meV, b) -10 meV, c) -40 meV, d) -70 meV.

Energy dispersion calculated for a = 5 nm, r = 5 nm in this case. In Figure 3.1, part a, for all s values bands are nearly the same that means V_0 is so small for distinguished bands. In part b, V_0 is enough to identify which band belongs to the corresponding s value. Dirac cones shapes begin to appear. When s = 0.1, the second band is above the Fermi level the other s values around the Fermi level there are three degenerate energy levels. In part c, Dirac cone shapes are better in this case s = 0.1 and s = 0.5 are pretty much same but s = 0.1 has highest energy split at Γ point. Different from Figure 3.1 parts a and b, the third and fourth bands are beyond the second band energies. In part d, s = 0.1 become important, at low potential values s dependency effect on band structure.

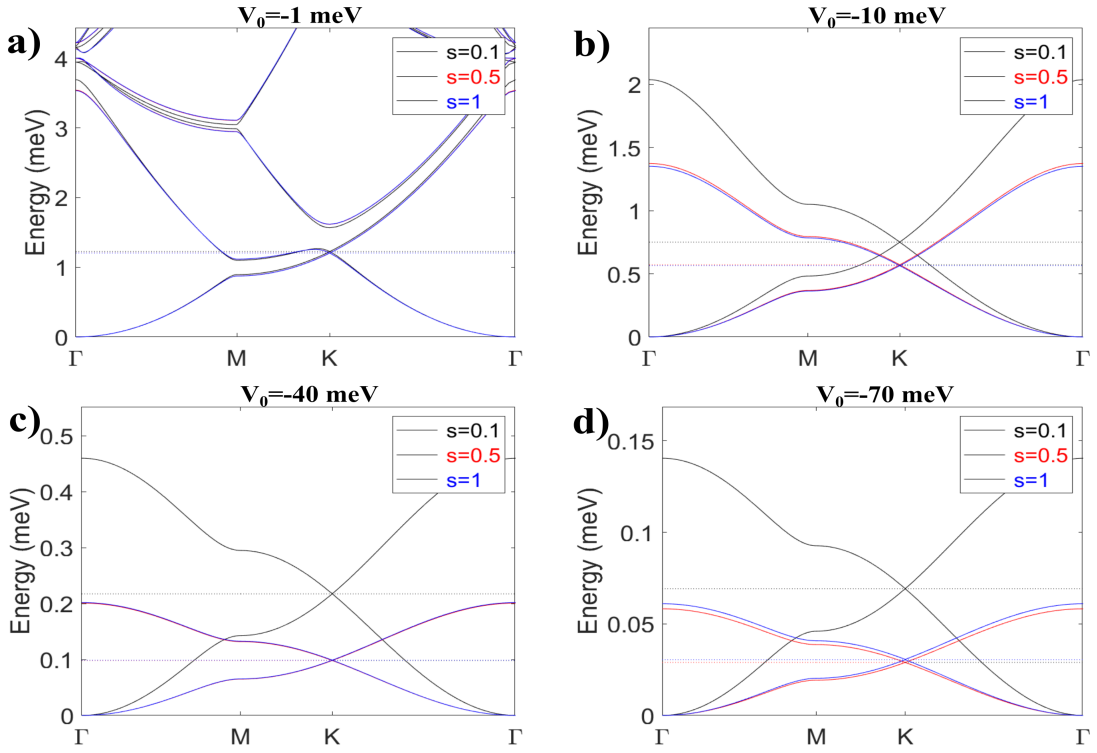

Figure 3.2. Band structures of dots with a = 50 nm, r = 20 nm. a) -1 meV, b) -10 meV, c) -40 meV, d) -70 meV.

In figure 3.2, parameters are a = 50 nm, r = 20 nm. In part, a same as in figure 3.1 part a, all bands overlap each other. In part b, Dirac cones appear and s = 0.5 and 1 has the same energy dispersion. Part c and d same as part b but Fermi level energy differences are getting bigger when the potential is getting lower. From part b, c and d, s = 0.1 different from other s values, that is rational because potential is softer. From Figure

2.1 s = 0.5 and 1 are pretty much same. Due to similar potential structure of s = 0.5 and 1 are correlate each other.

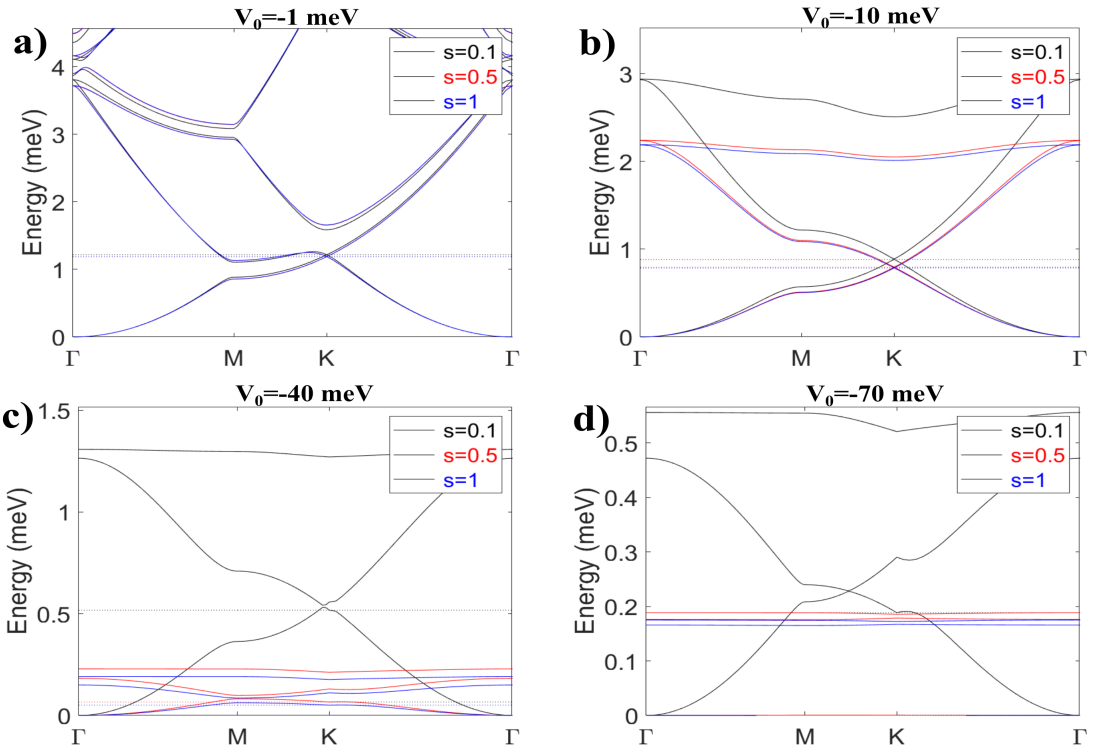

Figure 3.3. Band structures of dots with a = 50 nm, r = 30 nm. a) -1 meV, b) -10 meV, c) -40 meV, d) -70 meV.

Figure 3.3 parameters are a = 50 nm, r = 30 nm. This situation is an extreme case because the dot radius is greater than the dot to dot distance. That high radius means dots overlap each other. In part a, the potential is high so that there is barely a Dirac cone shape. In part b, Dirac cones appear and at K point Dirac cone shapes are so good. In parts c and d, Dirac cones are slipped through the M point. For all cases in this chapter s sensitivity plays a big role. Comparison between s = 0.1 and the others bands became nearly flat. In part d, Dirac cone sits between M and K point, and bands near the K point have an aggressive break.

Another important point of the extreme case is the energy dispersion look like antidot lattice energy dispersion. Band structure in Figure 3.3 and next chapter (Figure 4.1) have similar behavior at the third band. Overlaps of dots with soft edge potential look-alike as if there is an antidot at the center of honeycomb lattice with repulsive potential.

That might be used to model antidot lattice using dot lattice.

In all cases in this chapter, Dirac cones appear for some values. If the radius does not exceed to dot to dot distance a lot of opportunities to have Dirac cone shapely band structures. Interesting results are in extreme value. Dirac-like cones appeared but the lowest potential they moved through M point. Artificial graphene offers us to have Dirac cone or different band structures by changing dot to dot distances, radius, and potential. Besides those parameters, we add another parameter which is stiffness. In all figures, stiffness can change the band structure. Especially in Figure 3.1 d, stiffness plays a big role to achieve the Dirac cone. Another interesting result can be seen in Figure 3.3, while in part b all stiffness parameters result in Dirac cones. On the other hand, part d Dirac cones shifted between M and K points. Those results show us stiffness is an important parameter.

CHAPTER 4

BAND STRUCTURE OF ANTIDOT LATTICE FROM SINGLE-ELECTRON APPROXIMATION

In this section, the band structure of artificial graphene with antidots was examined using the single electron approximation. Band structures are calculated for b = 70 nm and r = 15, 30, 40 nm. Potential values are V_0 = 1, 6, 10 and 15 meV. s values are 0.1, 0.5, 1. The main goal of this chapter is to understand how different parameters affect band structure. Also, point out differences between dot lattice and antidot lattice energy dispersion.

Antidot lattice has repulsive potential to create honeycomb structures in low-energy areas. Solution of Scrödinger equation (equation 2.1) with antidot lattice vectors (equation 2.11) and k vectors (equation 2.14 and 2.15) results in band structure similar to the dot lattice band structure. In Figure 2.5, a comparison of the band structure obtained by our algorithm with another work.

The antidot concept is represented in Du et al. (2018). They compute numerical solutions and also fabricate artificial graphene with antidots. They achieved Dirac cone in energy dispersion (Figure 2.5). Using this information, examining another b, various radius and potential values are worth working on. In this case, only b = 70 nm is in this chapter. But this value is enough to understand the whole concept. Another effect on band structure is how stiffness value affects band structure. The soft potential may create a dot lattice with repulsive potential at the center of the honeycomb shape. That means creating dot lattice from antidot lattice is possible. Stiffness plays important role in this work. In chapter 3, we concluded that antidot lattice can be produced by dot lattice with extreme values. These transitional properties between dot lattice and antidot lattice may remove the physical barrier. Fabricating one type of lattice might be enough instead of fabricating two different lattices.

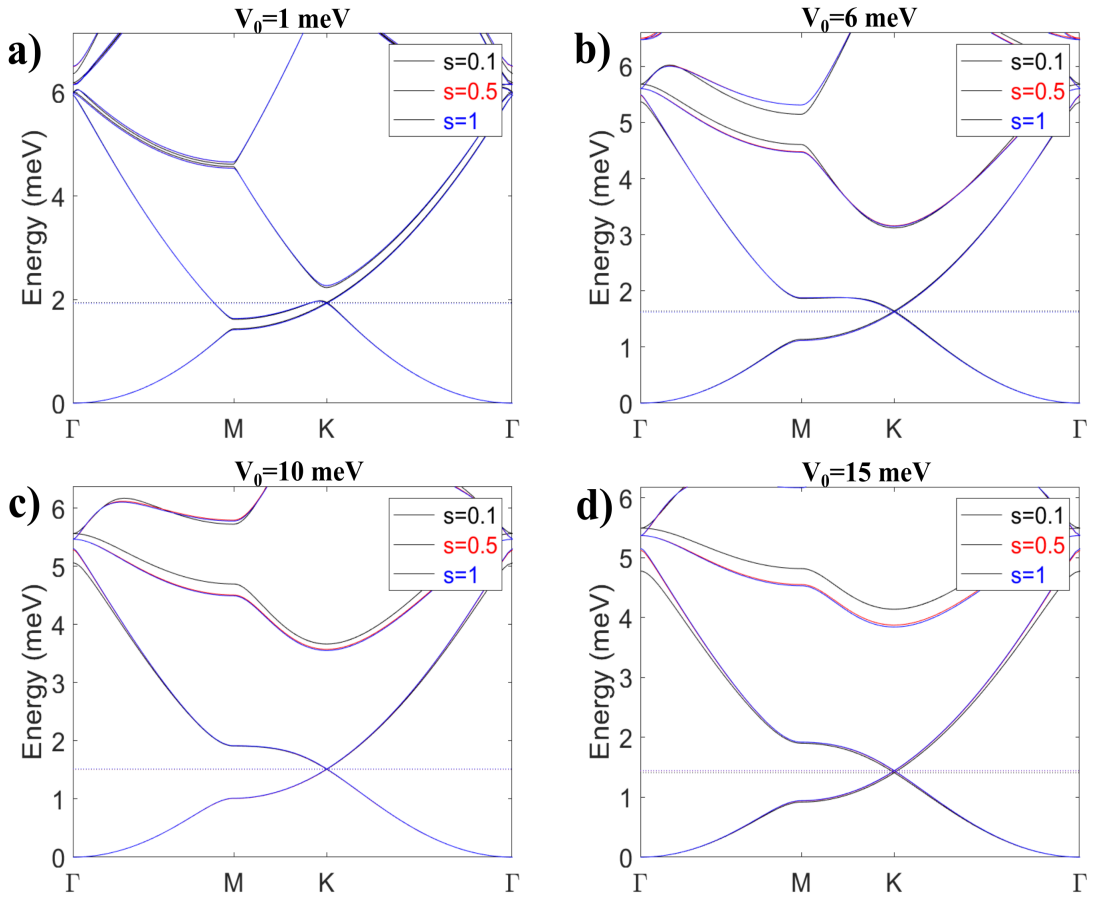

Figure 4.1. Band structures of antidots with $b = 70$ nm, $r = 15$ nm. a) 1 meV, b) 6 meV, c) 10 meV, d) 15 meV.

In Figure 4.1 part a, the potential is not high enough to create Dirac cones. In parts b, c and d are nearly the same. Stiffness values are not effective in this section. Γ point energies are also close to each other. Dirac cones start to appear from 6 meV. Dirac cones have the proper shape. Energies changes are very smooth between subfigures. Third band energies start near the second band-like in Figure 3.3.

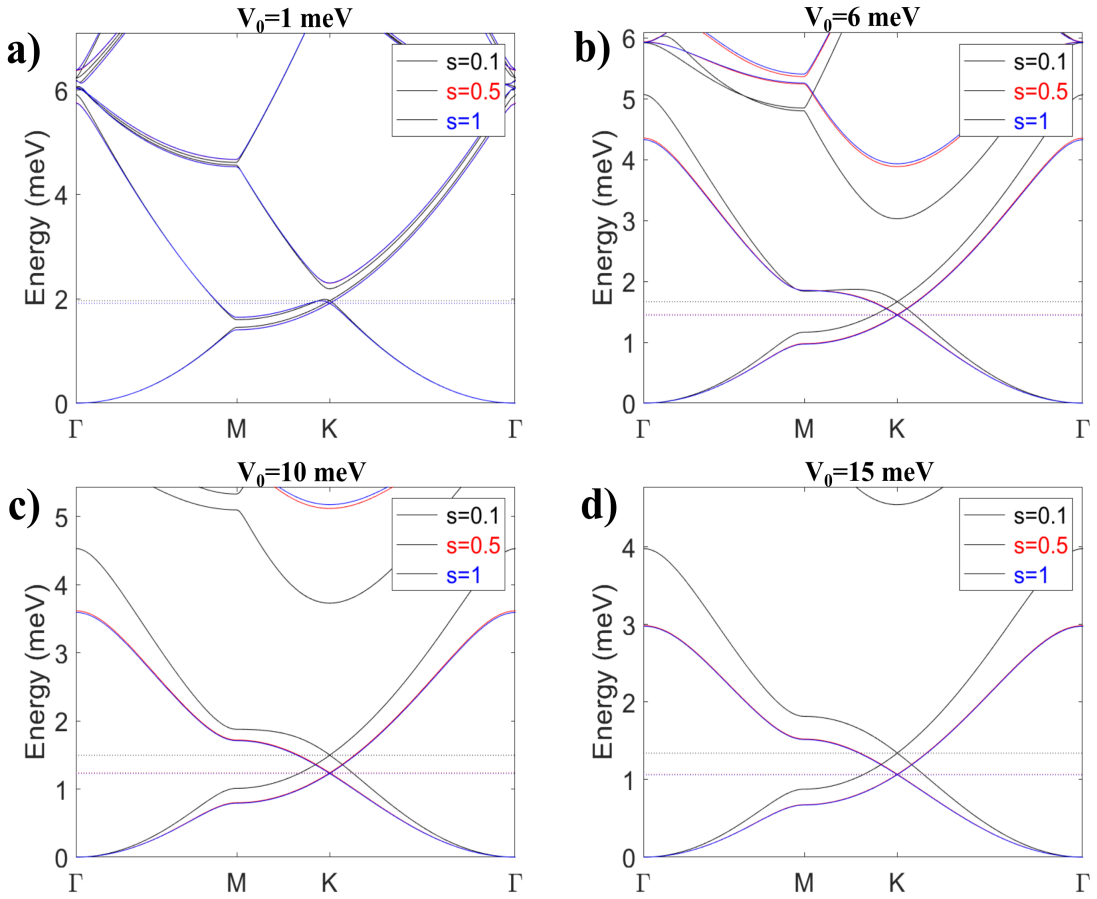

Figure 4.2. Band structures of antidots with $b = 70$ nm, $r = 30$ nm. a) 1 meV, b) 6 meV, c) 10 meV, d) 15 meV.

In Figure 4.2, Stiffness value become important for $b = 70$ nm, $r = 30$ nm with various potential. $s = 0.5$ and 1 result same energies at the first and second band. Γ point and Fermi level energies drop, when the potential increases. These results are expected results from dot lattice energy dispersion figures. Dirac cones appeared at b, c and d. Those Dirac cones have the proper shape. $s = 0.1$ has different band structure.

In Figure 4.3, extreme cases are examined like in dot lattice. At this point, there are no Dirac cones. This is not a surprise because overlapping antidots trap electrons where the potential is minimum. This requires high energy to jump another band.

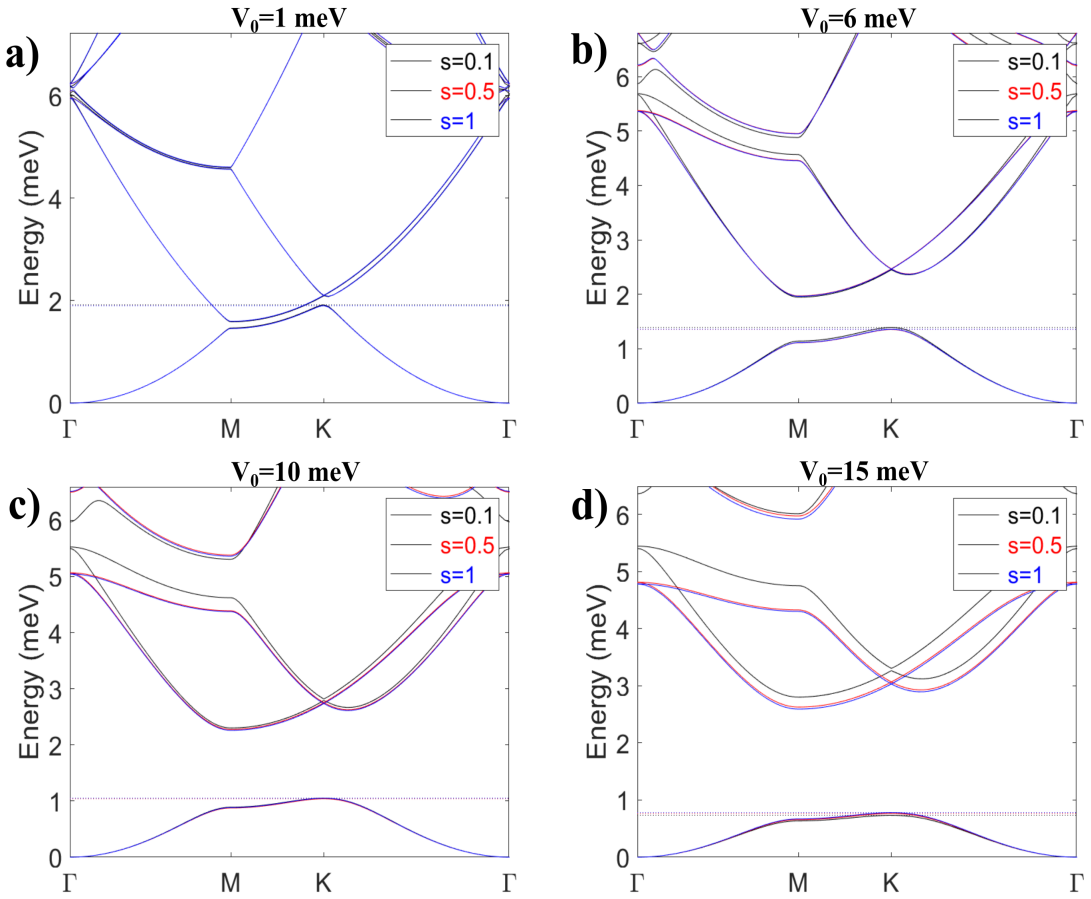

Figure 4.3. Band structures of antidots with $b = 70$ nm, $r = 40$ nm. a) 1 meV, b) 6 meV, c) 10 meV, d) 15 meV.

In this chapter, the antidot lattice band structure examined, some values result in Dirac cones. Dirac cones result of honeycomb structure, antidot lattice with repulsive potential yields this feature. Artificial graphene with antidot consists of repulsive potential. Those potentials are arranged in a triangular lattice shape. Low potential areas have a similar structure to a honeycomb lattice. Using this feature, the solution of Schrödinger's equation for antidot lattice results in Dirac cones. In this part, except for extreme value, Dirac cone shape achieved. Changing radius does not affect energies. The main reason is radius does not change the honeycomb shape distances created at low energy areas. Extreme cases have gaps rather than Dirac cones. Radius exceed antidot to antidot distances so that the lattice structure became different from the triangular lattice. That is why Dirac cones do not appear in this case.

CHAPTER 5

TIGHT-BINDING AND HUBBARD PARAMETERS

5.0.1. Dot Lattice

Graphene's value of t is -2.8 eV (Castro Neto et al. (2009)). Artificial graphene's hopping parameters are smaller than $|-2.8|$ eV. This outcome is expected due to larger distances between dots. When the potential decreases, in band structures, energy splits become smaller at Γ points. That means the slope of the second band near the K point is decreasing, this result in small t values. In table 5.1, s = 0.1 has always high value of t, when the potential decreases t values become smaller for same dot to dot distance and radius. Hubbard U values increase while s values increase.

t(meV)	Hubbard U (meV)	stiffnes(s)	Potential(meV)	Distance(nm)	Radius(nm)
0.136966	12.8318	0.1	-40	50	5
0.054373	18.4217	0.5	-40	50	5
0.048615	19.309	1	-40	50	5
0.037045	16.7266	0.1	-70	50	5
0.003626	21.1143	0.5	-70	50	5
0.003390	21.1301	1	-70	50	5
0.076664	16.319	0.1	-40	50	20
0.034174	26.9924	0.5	-40	50	20
0.034226	28.6794	1	-40	50	20
0.023325	15.6539	0.1	-70	50	20
0.009903	13.5226	0.5	-70	50	20
0.010232	13.233	1	-70	50	20

Table 5.1. Hopping t and Hubbard U parameters of dots.

5.0.2. Antidot Lattice

Some t values are calculated for antidots. Unfortunately modeling single antidot for to solve Hubbard U is hard to achive. In table 5.2, there is no significant change in t parameters among $b = 50$ nm and also $b = 60$. The parameter b is related to a parameter in dot lattice, which is $a = b/\sqrt{3}$. Due to this relation, t parameters are between 0.62 and 0.65. In table 5.2, $b = 50$ nm, using $a = b/\sqrt{3}$ results $a = 28.8675$ nm, for $b = 60$ nm resulting parameter of a is 34.641 nm.

t(meV)	stiffness(s)	Potential(meV)	Distance(nm)	Radius(nm)
0.650952	0.1	1	50	5
0.651052	0.5	1	50	5
0.651038	1	1	50	5
0.649054	0.1	10	50	5
0.650840	0.5	10	50	5
0.650736	1	10	50	5
0.647482	0.1	15	50	5
0.650705	0.5	15	50	5
0.650575	1	15	50	5
0.649949	0.1	1	50	15
0.650474	0.5	1	50	15
0.650266	1	1	50	15
0.634607	0.1	10	50	15
0.635388	0.5	10	50	15
0.633790	1	10	50	15
0.623622	0.1	15	50	15
0.625394	0.5	15	50	15
0.623527	1	15	50	15
0.452103	0.1	1	60	5
0.452120	0.5	1	60	5
0.452114	1	1	60	5
0.451141	0.1	10	60	5
0.451996	0.5	10	60	5
0.451957	1	10	60	5
0.450199	0.1	15	60	5
0.451927	0.5	15	60	5
0.451882	1	15	60	5

Table 5.2. Hopping t parameters of antidots.

In this chapter, t and U values are investigated. These parameters are important to solve tight-binding and mean-field Hubbard equations for finite-sized structures, as well as to provide input to QMC. In this work dot and antidot lattice are bulk. Using those parameters finite lattices' electronic properties can be calculated. It is important to compare graphene and artificial graphene t and U values because those parameters are related to magnetic properties such as by using mean-field Hubbard spins involved in Hamiltonian and magnetic properties can be calculated. There are a lot of works for calculated U values for graphene (Sorella and Tosatti (1992);Fernández-Rossier and Palacios (2007);Pisani et al. (2007);Yazyev (2010);Thomann et al. (1985)). Also t values are related to electron velocity near K point. These values are important because the semimetallic behavior of graphene is the result of electron velocity. Another important point of t is the tight-binding method. This method works very well in graphene. Using table 5.1 and 5.2 tight-binding calculations can be computed.

CHAPTER 6

BAND STRUCTURE OF DOTS LATTICE FROM DENSITY FUNCTIONAL THEORY

However, often in chapter 3 using single-electron solutions, the band structure of dot lattice is studied. Single-electron approximation is not enough to have accurate information about electronic properties of material. Many electron solutions are essential to understand electron-electron interactions, spins and magnetic properties. DFT is the method which many electron features can be calculated. While many DFT packages exist for realistic 3D calculations. There are no 2D DFT algorithm packages for semiconductor systems so that we wrote DFT algorithm to calculate many electron effect.

In this chapter, energy dispersion of artificial graphene with dot lattice is examined by solving Kohn-Sham equation. Single-electron solutions and DFT solutions are compared. As another extreme case added in this work which is $s = 0.01$ stiffness value.

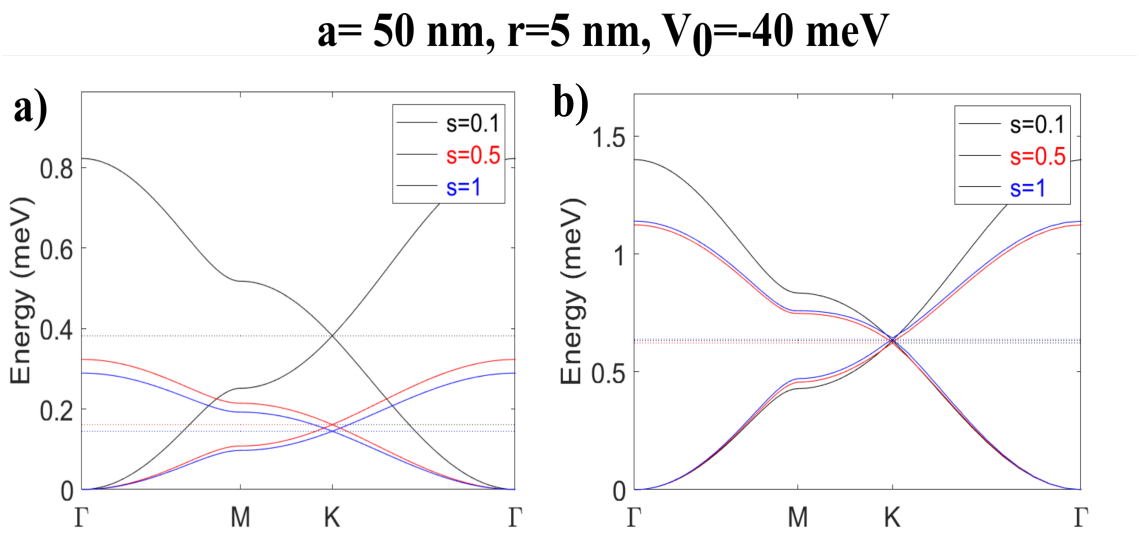

Figure 6.1. Band structures of dots with $a = 50$ nm, $r = 5$ nm, V_0 =-40 meV. a) Single-electron approximation solution b) DFT solution.

In figure 6.1, single-electron bands have low energies both Fermi level and Γ

points beside that DFT bands are high energies in both way. In figure a, s = 0.5 and 1 look like collapsed and s = 0.1 illustrates a different band energies. In Figure 6.1 b, s sensitivity do not play much important role as in single-electron case. But s = 0.1 still have different energies. Figure 6.1 shows that, adding electron-electron interaction splits bands for all stiffness.

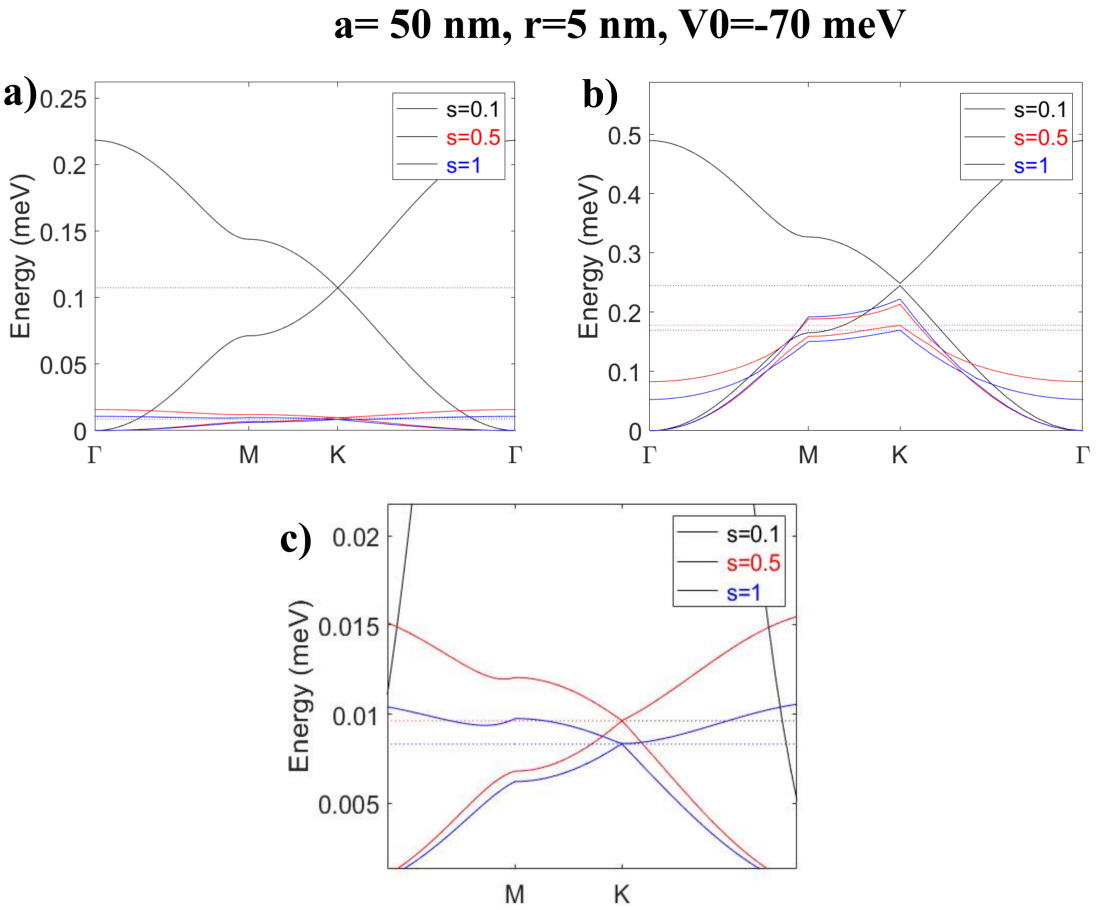

Figure 6.2. Band structures of dots with a = 50 nm, r = 5 nm, V_0 = -70 meV. a) Single-electron approximation solution b) DFT solution c) s = 0.5 and 1 band structures at figure a

In figure 6.2, Band structures have Dirac cones as can be seen at figure a and b. Bands are distorted while s= 0.5 and 1. Low potential energies DFT solutions look like s sensitive. Adding Coulomb interactions and Exchange-Correlation potential might change the shape of the honeycomb lattice at hard s values. In figure b, when the s= 0.1, Dirac cone appears with a little gap at K point. As can be seen in Figure 6.2 s sensitivity is very important

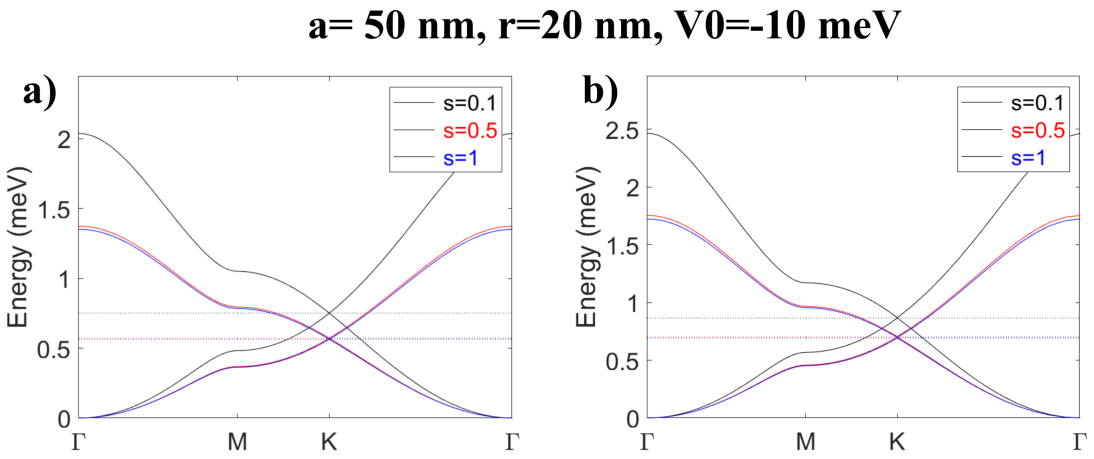

Figure 6.3. Band structures of dots with a = 50 nm, r = 20 nm, V_0 = -10 meV. a) Single-electron approximation solution b) DFT solution.

In Figure 6.3, both figures show that optimal potential and radius values to obtain Dirac cones for all stiffness parameters. DFT shifts energies to upward. In both cases, figures have undistorted and clean Dirac cones.

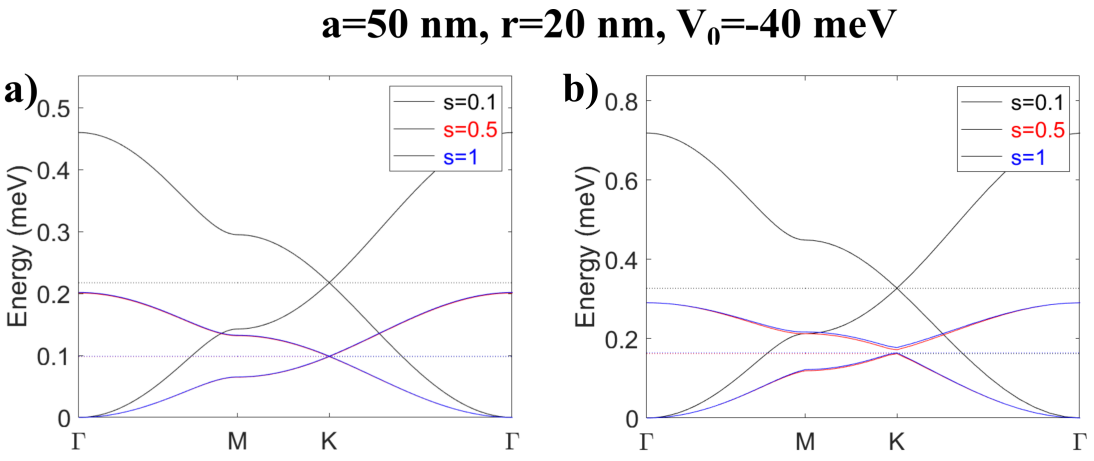

Figure 6.4. Band structures of dots with a = 50 nm, r = 20 nm, V_0 = -40 meV. a) Single-electron approximation solution b) DFT solution.

In Figure 6.4, second band of s = 0.5 and 1 are tend to linear in DFT figures. Both figures look like same except energies are higher in DFT solutions.

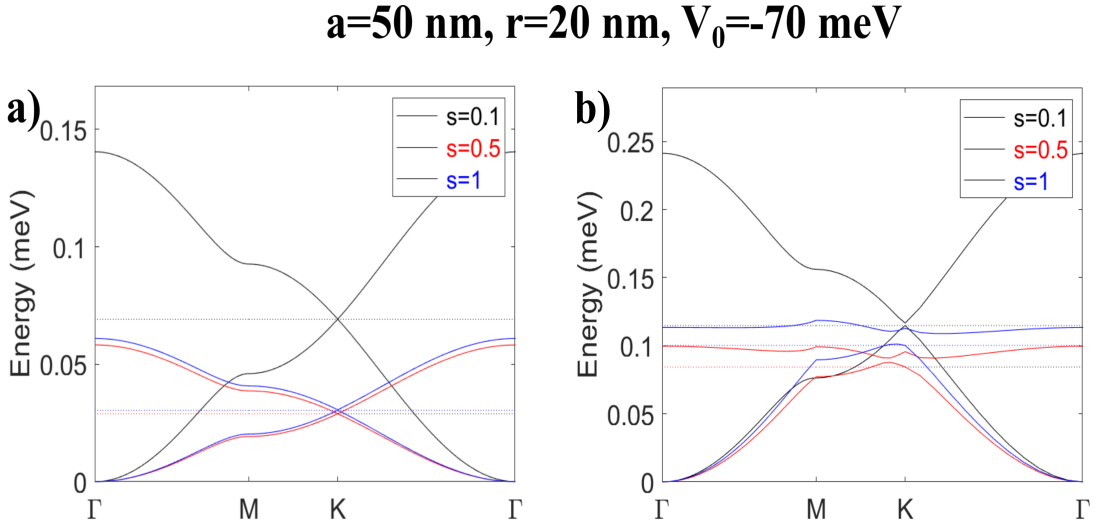

Figure 6.5. Band structures of dots with a = 50 nm, r = 20 nm, V_0 = -70 meV. a) Single-electron approximation solution b) DFT solution.

In Figure 6.5 part b, like in the figure 6.2, at lowest potential makes s sensitive system. First band of s = 1 look alike a band form up Dirac cone system but second band is nearly flat. The one can say same things for s = 0.5 but at least it almost forms Dirac cone shape. s = 1 has Dirac cone with a small gap at K point like in figure 6.2. So far we have seen that stiffness can used as fourth parameter in artificial graphene. Artificial graphene already gives us opportunity to freely build lattice. Adding stiffness gives us a lot of new chance to have more band structures.

Another work done in DFT part is checking the s = 0.05 and comparing with single-electron case. Some of the parameters are changed for understand the whole work and add another perspective. Dot to dot distance is chosen 50 nm, radius are 10, 20, 30 nm and potentials are -50.5, -25, -15.5 meV. Those potentials came from QMC solutions. In QMC finite structure was calculated. So that we sought charge neutrality in QMC. DFT solutions of those parameters are investigated and Dirac cones appeared in energy dispersion but Dirac cones positioned between M and K points. Also DFT solutions compared with single-electron solutions.

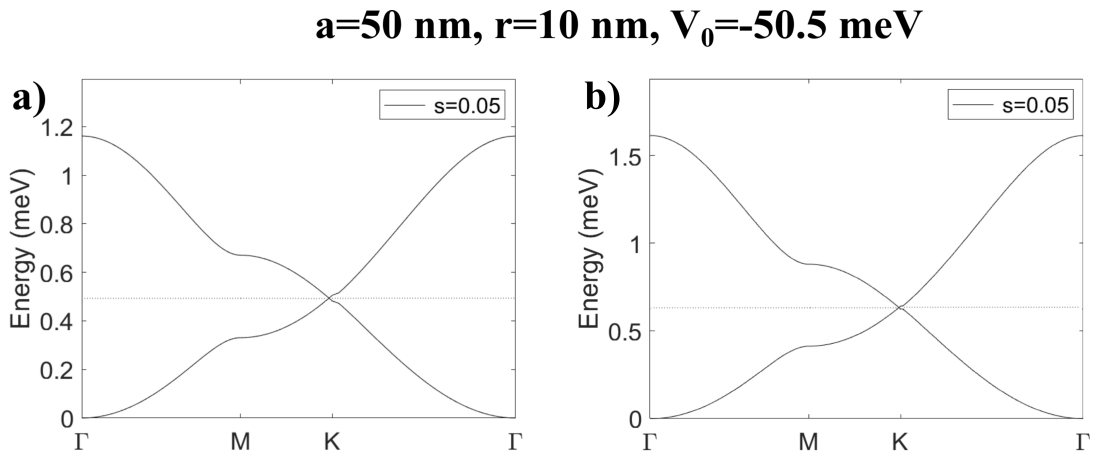

Figure 6.6. Band structures of dots with a = 50 nm, r = 10 nm, V_0 = -50.5 meV. a) Single-electron approximation solution b) DFT solution.

In figure 6.6, Dirac cone moved between M and K points in single-electron bands, on the other hand, Dirac cone close to K point. Energy split at Γ point high in DFT solutions.

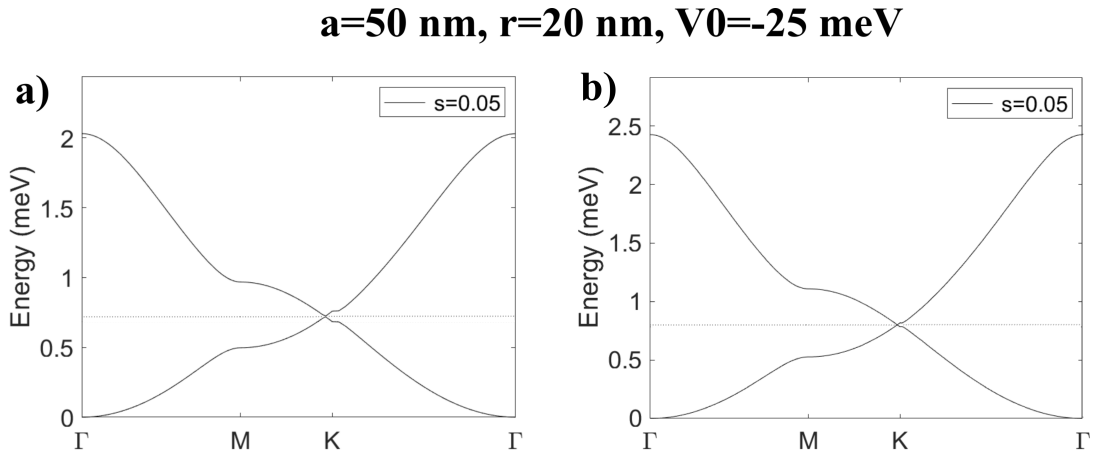

Figure 6.7. Band structures of dots with a = 50 nm, r = 20 nm, V_0 = -25 meV. a) Single-electron approximation solution b) DFT solution.

In figure 6.7, gap at K point become small in figure b. Bands near K point became smooth in DFT case.

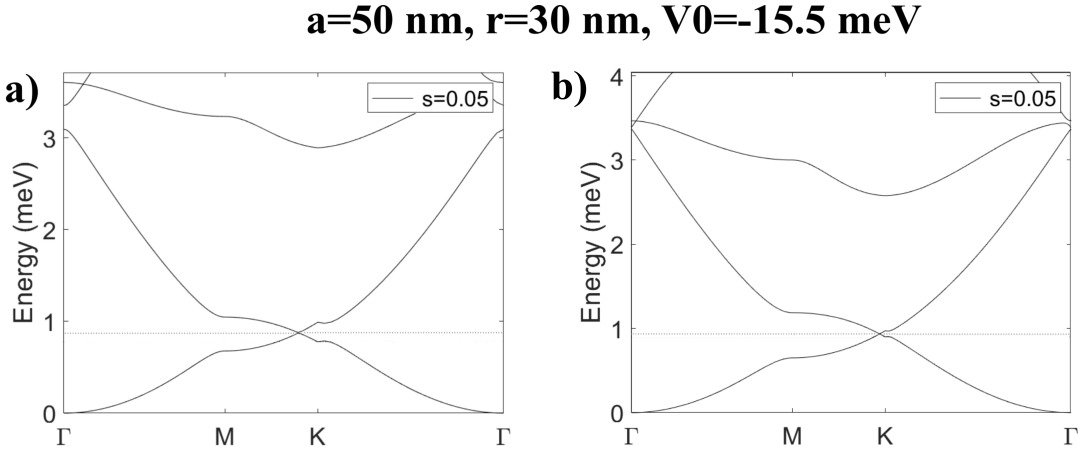

Figure 6.8. Band structures of dots with a = 50 nm, r = 30 nm, V_0 = -15.5 meV. a) Single-electron approximation solution b) DFT solution.

In figure 6.8, radius is 30 nm and this is an extreme case. In DFT case near K point bands are smooth. Gap between bands are small at K point.

For all cases, DFT solutions are much more realistic than single-electron solutions. In real systems, electrons interact with each other and with the environment. Adding interactions in the Hamiltonian cause much more realistic energies than single-electron energies. Dirac cones are achieved in all DFT cases. Also, nearly flat bands appeared. Stiffness changes energies. Both single-electron and DFT show us stiffness is an important parameter.

CHAPTER 7

TIGHT-BINDING PARAMETERS

t_{DFT}(meV)	t_{single}(meV)	stiffnes(s)	Potential(meV)	Distance(nm)	Radius(nm)
0.240337	0.17877	0.05	-50.5	50	10
0.305309	0.26320	0.05	-25	50	20
0.319038	0.26181	0.05	-15.5	50	30

Table 7.1. Hopping t parameters of dots obtained from DFT solutions. Comparison between single electron solutions.

As can be seen at table 6.1, DFT t values higher than single-electron approximation. This is expected because first and second band split in DFT solutions. Reason behind the negative t value is the first band slope become negative due to distorted Dirac cone shape.

t_{DFT}(meV)	stiffnes(s)	Potential(meV)	Distance(nm)	Radius(nm)
0.247029	0.1	-40	50	5
0.214441	0.5	-40	50	5
0.204905	1	-40	50	5
0.104592	0.1	-70	50	5
0.049018	0.5	-70	50	5
0.059182	1	-70	50	5
0.342187	0.1	-10	50	20
0.335410	0.5	-10	50	20
0.280726	1	-10	50	20
0.121686	0.1	-40	50	20
0.059906	0.5	-40	50	20
0.062366	1	-40	50	20
0.035290	0.1	-70	50	20
0.020730	0.5	-70	50	20
0.033854	1	-70	50	20

Table 7.2. Hopping t parameters of dots obtained from DFT solutions. Comparison between single electron solutions.

Table 7.2 have t values comes from the DFT solutions. Those t values are higher comparing with table 5.1. Adding interactions separate first and second band energies that is the reason for high t values.

In this chapter DFT band structures studied and compared with single electron approximation. DFT solutions are work well in parameters obtained from single dot section. DFT solutions are also promising for extreme values because proper Dirac cone appears in DFT case rather than single electron case. In studying extreme , it can be used as antidot with honeycomb shape with antidot and in DFT, extreme values has clean Dirac cone shape.

CHAPTER 8

CONCLUSION

Starting from Bloch's theorem, the relationship between real space and momentum space and fundamental equations were applied on this work. Understanding momentum space was important because the band structure of a material is calculated in momentum space. Graphene has an idiosyncratic band structure, this is the consequence of honeycomb structure. Using this structure artificial graphene was built by dot and antidot lattice. The tangent-hyperbolic function was used to model dot and antidot potential.

The single-electron approximation was used to obtain the initial band structure. Some of them have Dirac cones. This outcome was expected due to the honeycomb configuration. In both dot and antidot cases, stiffness parameter was applied to understand how s influences bands. $s = 0.5$ and 1 yield nearly the same energies. Band structure of $s = 0.1$ was different from them because in Figure 2.1 smooth potential slowly varied to zero. Single-electron t values were calculated to obtain hopping parameters and compared with Graphene. Hubbard U values were also studied. U/t values are high besides graphene.

There are a lot of package programs to calculate DFT solutions for atoms, molecules, etc., such as Quantum Espresso, VASP, Gaussian, but those programs are mostly 3D. We could not find a package program to compute a 2D semiconductor-based DFT program. We decided that writing the algorithm is the best choice for us. Using the algorithm which we wrote, we calculated single electron and DFT energies. In DFT, the energy split at Γ point is higher than in the Single-electron case. That means, t values are higher in DFT solutions. In previous chapters, extreme cases were when the r is greater than a or b distances. Another extreme case was added in the DFT part which was $s = 0.05$ and calculated for both methods. In $s = 0.05$ situation, Dirac cones moves back through K point in DFT, single-electron case Dirac cones nearly middle of M and K point. An important subject overall thesis is stiffness parameter. The stiffness parameter was added in the tangent-hyperbolic function to control the stiffness of potential. Artificial graphene allows us to tune the parameters. Those parameters are dot to dot or antidot to antidot

distance, the radius of the dot, and potential. Adding the fourth parameter in those parameters results in a lot of band structure. Freedom of choice of parameters makes artificial graphene a valuable subject to investigate.

Artificial graphene has another kind of special property. In figures, the reader can see that a lot of band structure types occurred beside the Dirac cone-shaped band structures. Same dot to dot distance, radius, and stiffness value but different potential result wide range of band structure. Metaphorically, changing one parameter yields a universe.

REFERENCES

Arfken, G. B. and H. J. Weber (2005). *Mathematical methods for physicists; 6th ed.* Academic Press.

Ashcroft, N. W. and N. D. Mermin (1976). *Solid State Physics*.

Bagayoko, D. (2014). Understanding density functional theory (DFT) and completing it in practice. *AIP Advances 4*(12).

Balandin, A. A., S. Ghosh, W. Bao, I. Calizo, D. Teweldebrhan, F. Miao, and C. N. Lau (2008). Superior thermal conductivity of single-layer graphene. *Nano Letters 8*(3), 902–907.

Berger, C., Z. Song, T. Li, X. Li, A. Y. Ogbazghi, R. Feng, Z. Dai, A. N. Marchenkov, E. H. Conrad, P. N. First, and W. A. de Heer (2004). Ultrathin epitaxial graphite 2d electron gas properies and a route toward graphene-based nanoelectronics. *The Journal of Physical Chemistry B 108*(52), 19912–19916.

Bunch, J. S., S. S. Verbridge, J. S. Alden, A. M. Van Der Zande, J. M. Parpia, H. G. Craighead, and P. L. McEuen (2008). Impermeable atomic membranes from graphene sheets. *Nano Letters 8*(8), 2458–2462.

Castro, A., E. Räsänen, and C. A. Rozzi (2009). Exact Coulomb cutoff technique for supercell calculations in two dimensions. *Physical Review B - Condensed Matter and Materials Physics 80*(3), 1–4.

Castro Neto, A. H., F. Guinea, N. M. R. Peres, K. S. Novoselov, and A. K. Geim (2009, Jan). The electronic properties of graphene. *Rev. Mod. Phys. 81*, 109–162.

Du, L., S. Fallahi, S. Wang, G. C. Gardner, L. N. Pfeiffer, M. J. Manfra, S. J. Wind, K. W. West, A. Pinczuk, D. Scarabelli, and V. Pellegrini (2018). Emerging many-body effects in semiconductor artificial graphene with low disorder. *Nature Commu-*

nications 9(1), 1–6.

Fernández-Rossier, J. and J. J. Palacios (2007). Magnetism in graphene nanoislands. *Physical Review Letters 99*(17), 1–5.

Fiorillo, M., A. F. Verre, M. Iliut, M. Peiris-Pagés, B. Ozsvari, R. Gandara, A. R. Cappello, F. Sotgia, A. Vijayaraghavan, and M. P. Lisanti (2015). Graphene oxide selectively targets cancer stem cells, across multiple tumor types: Implications for non-toxic cancer treatment, via "differentiation-based nano-therapy". *Oncotarget 6*(6), 3553–3562.

Gibertini, M., A. Singha, V. Pellegrini, M. Polini, G. Vignale, A. Pinczuk, L. N. Pfeiffer, and K. W. West (2009). Engineering artificial graphene in a two-dimensional electron gas. *Physical Review B - Condensed Matter and Materials Physics 79*(24), 8–11.

Gomes, K. K., W. Mar, W. Ko, F. Guinea, and H. C. Manoharan (2012). Designer Dirac fermions and topological phases in molecular graphene. *Nature 483*(7389), 306–310.

Guclu A.D., Potasz P., K. M. H. P. (2014). *Graphene Quantum Dots*. Springer.

Hashimoto, A., K. Suenaga, A. Gloter, K. Urita, and S. Iijima (2004). Direct evidence for atomic defects in graphene layers. *Nature 430*(7002), 870–873.

Hohenberg, P. and W. Kohn (1964, nov). Inhomogeneous Electron Gas. *Physical Review 136*(3B), B864–B871.

Ihn, T., J. Güttinger, F. Molitor, S. Schnez, E. Schurtenberger, A. Jacobsen, S. Hellmüller, T. Frey, S. Dröscher, C. Stampfer, and K. Ensslin (2010). Graphene single-electron transistors. *Materials Today 13*(3), 44–50.

Juang, Z.-Y., C.-Y. Wu, A.-Y. Lu, C.-Y. Su, K.-C. Leou, F.-R. Chen, and C.-H. Tsai (2010). Graphene synthesis by chemical vapor deposition and transfer by a roll-to-roll process. *Carbon 48*(11), 3169 – 3174.

Kaxiras, E. (2003). *Atomic and Electronic Structure of Solids*. Cambridge University Press.

Kohn, W. and L. J. Sham (1965, nov). Self-Consistent Equations Including Exchange and Correlation Effects. *Physical Review 140*(4A), A1133–A1138.

Kul, E. B., M. Polat, and A. D. Güçlü (2020). Electronic and magnetic properties of graphene quantum dots with two charged vacancies. *Solid State Communications 322*.

Lee, C., X. Wei, J. W. Kysar, and J. Hone (2008). Measurement of the elastic properties and intrinsic strength of monolayer graphene. *Science 321*(5887), 385–388.

Manfra, M. J., L. N. Pfeiffer, V. Pellegrini, A. Pinczuk, K. West, S. Wang, G. C. Gardner, S. J. Wind, Y. Y. Kuznetsova, and D. Scarabelli (2015). Fabrication of artificial graphene in a GaAs quantum heterostructure. *Journal of Vacuum Science and Technology B, Nanotechnology and Microelectronics: Materials, Processing, Measurement, and Phenomena 33*(6), 06FG03.

Marder, M. P. (2010). *Condensed Matter Physics*. Wiley.

Novoselov, K. S., A. K. Geim, S. V. Morozov, D. Jiang, Y. Zhang, S. V. Dubonos, I. V. Grigorieva, and A. A. Firsov (2004). Electric field effect in atomically thin carbon films. *Science 306*(5696), 666–669.

Parr, R. G. and W. Yang (1989). *Density-Functional Theory of Atoms and Molecules*. Oxford University Press.

Pisani, L., J. A. Chan, B. Montanari, and N. M. Harrison (2007). Electronic structure and magnetic properties of graphitic ribbons. *Physical Review B - Condensed Matter and Materials Physics 75*(6).

Priyadarsini, S., S. Mohanty, S. Mukherjee, S. Basu, and M. Mishra (2018). Graphene and graphene oxide as nanomaterials for medicine and biology application. *Journal of Nanostructure in Chemistry 8*(2), 123–137.

Radchenko, T. M., V. A. Tatarenko, I. Y. Sagalianov, and Y. I. Prylutskyy (2014). Configurations of structural defects in graphene and their effects on its transport properties. *Graphene: Mechanical Properties, Potential Applications and Electrochemical Performance*, 219–259.

Reina, A., X. Jia, J. Ho, D. Nezich, H. Son, V. Bulovic, M. S. Dresselhaus, and J. Kong (2009). Large area, few-layer graphene films on arbitrary substrates by chemical vapor deposition. *Nano Letters 9*(1), 30–35.

Savvas, D. and G. Stefanou (2018). Determination of random material properties of graphene sheets with different types of defects. *Composites Part B: Engineering 143*(April), 47–54.

Sorella, S. and E. Tosatti (1992, aug). Semi-metal-insulator transition of the hubbard model in the honeycomb lattice. *Europhysics Letters (EPL) 19*(8), 699–704.

Staneva, A. D., D. K. Dimitrov, D. N. Gospodinova, and T. G. Vladkova (2021). Antibiofouling activity of graphene materials and graphene-based antimicrobial coatings. *Microorganisms 9*(9), 1–20.

Tanatar, B. and D. M. Ceperley (1989, mar). Ground state of the two-dimensional electron gas. *Physical Review B 39*(8), 5005–5016.

Thomann, H., L. K. Dalton, M. Grabowski, and T. C. Clarke (1985). Direct observation of Coulomb correlation effects in polyacetylene. *Physical Review B 31*(5), 3141–3143.

Tian, W., W. Li, W. Yu, and X. Liu (2017). A review on lattice defects in graphene: Types generation effects and regulation. *Micromachines 8*(5).

Wallace, P. R. (1947, May). The band theory of graphite. *Phys. Rev. 71*, 622–634.

Wang, S., D. Scarabelli, L. Du, Y. Y. Kuznetsova, L. N. Pfeiffer, K. W. West, G. C. Gardner, M. J. Manfra, V. Pellegrini, S. J. Wind, A. Pinczuk, D. Scarabelli, A. Pinczuk, S. J. Wind, G. C. Gardner, V. Pellegrini, L. Du, Y. Y. Kuznetsova, M. J. Manfra, L. N.

Pfeiffer, K. W. West, G. C. Gardner, M. J. Manfra, V. Pellegrini, S. J. Wind, and A. Pinczuk (2017, jan). Observation of Dirac bands in artificial graphene in small-period nanopatterned GaAs quantum wells. *Nature Nanotechnology 13*(1), 29–33.

Wunsch, B., F. Guinea, and F. Sols (2008). Dirac-point engineering and topological phase transitions in honeycomb optical lattices. *New Journal of Physics 10*.

Yazyev, O. V. (2010). Emergence of magnetism in graphene materials and nanostructures. *Reports on Progress in Physics 73*(5).